^{161}HO + IUDR:

OPTIMIZED PHOTON ACTIVATION THERAPY

By

Bryan J. Stephens

Dissertation

Submitted to the Faculty of the

Graduate School of Vanderbilt University

in partial fulfillment of the requirements

for the degree of

DOCTOR OF PHILOSOPHY

in

Physics

August, 2010

Nashville, Tennessee

Approved:

Professor Marcus H. Mendenhall, Chair

Professor Charles W. Coffey II

Professor Richard F. Haglund Jr

Professor Michael G. Stabin

Professor Robert A. Weller

ACKNOWLEDGEMENTS

TABLE OF CONTENTS

LIST OF TABLES

LIST OF FIGURES

CHAPTER I

INTRODUCTION AND MOTIVATION

Cancer is a pandemic as widespread as any major disease, affecting millions around the world, and though some research in cancer therapy is aimed at preventative measures and strengthening the immune system to recognize and combat it, the vast majority of research is an exercise in cell killing. Good therapeutic techniques are both selective and efficient, sparing healthy tissue and using as little foreign intervention in the body as possible; most fall in two primary modalities: chemo- and radiation therapy.

Chemotherapy, at its heart, is the ingestion of poison: toxic pharmaceuticals that scientists attempt to design with tumors cells as their target. Discoveries in biology, chemistry, and pharmacology have led to hundreds of new drugs that have advanced this modality to, in many cases, an oncologist's first choice in cancer treatment. Fundamentally though, the development of these techniques is predicated on finding ways in which cancer cells are different from normal cells, whether it be an over- or under-expression of certain antibodies or enzymes. The fact remains that there are millions of such minute differences among various types of normal cells, never-mind between them and cancer cells. Even more challenging is the fact that within a certain class of cancer, breast cancer for example, there is huge variation of biological composition and so dedicated treatments for one variant could be completely useless for others. Furthermore, any single mutation of a normal cell can form a cancerous one that will proliferate and spread, so identifying these small number of mutations in our enormous genome is a daunting task.

Radiation therapy depends much less on cancer biology and human physiology and so its effects can be more easily predicted and its administration more readily controlled. Once the tumor is identified as cancer, usually by the physician after analysis of a biopsy, and located with millimeter accuracy by computed tomography (CT) (or alternative diagnostic scan), the medical physicist can use an arsenal of treatment planning software and particle accelerators to deliver a lethal dose of radiation to the target volume with strict limitations on the dose to peripheral, healthy tissue. There are various techniques in radiation therapy, all of which aim to control the homogeneity of dose within the tumor as well as the limitation of dose elsewhere. Much of the methodology revolves around the idea that dose is additive and so at the intersection of two beams the dose is amplified while along the track of each individual beam, dose is limited. Use of enough beams at distinct angles can provide sufficient cumulative dose to the tumor volume, but even though the dose along each track is minimal compared to the tumor's, many healthy organs will have been exposed to some radiation along these paths. Intensity modulated and image guided radiotherapy (IMRT and IGRT) in their various forms are the current state-of-the-art solution to this dilemma. Current accelerators house pneumatic collimators, robotic arms, and on board monitoring systems to meticulously control the shape, intensity, and direction of the radiation beam to fit the pre-planned dose distribution criteria. Though huge advances in these technologies have led to much clinical success, they still share an inherent flaw.
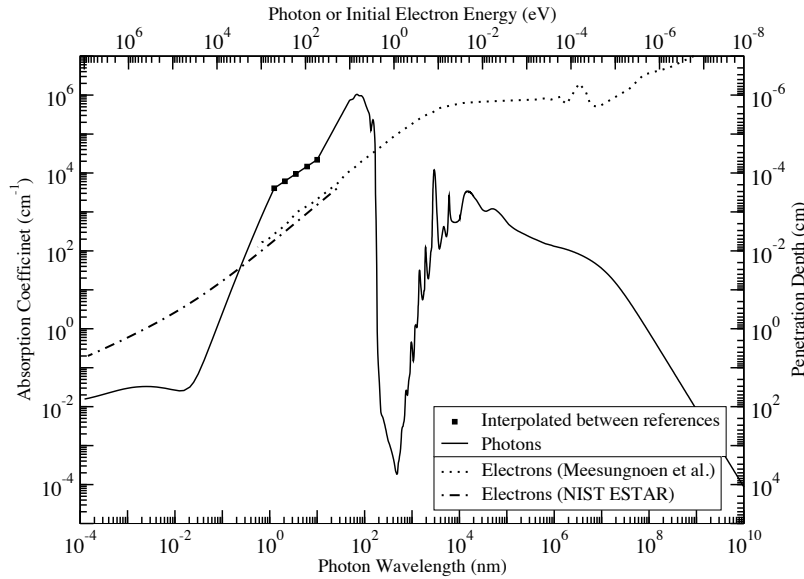
Figure 1.1: Absorption coefficients and corresponding penetration depths of photons and electrons in water across the spectrum. Photon data is linear interpolated between data 1.24 nm - 124 fm (Seltzer, 1993) and 10 - 10^{10} nm(Segelstein, 1981; Querry et al., 1991). For photons, actual data are mass-energy absorption coefficients and penetration depth is defined as the 1/e value. For electrons, data are penetration depths as calculated in the constant slow down approximation (CSDA) (Berger et al., 2008; Meesungnoen et al., 2002).

1.1 The Hazards of Targeting Water

The human cell is comprised primarily of water. The majority of radiotherapy techniques use megavoltage radiation, whether photons or electrons, for the penetration power. Figure 1.1 shows the absorption and penetration of photons and electrons in water throughout the spectrum. Except for photons in the visible spectrum, water is *most* transparent in the megavoltage range for both types of radiation. While wielding the ability to access tumors at significant depth in the body, fundamentally, these techniques surrender to the weakest possible absorption mechanism. Consequently, extremely high flux is necessary in accelerators to deliver a sufficient number of photons to achieve prescribed doses.

With absorption in mind, people have also experimented in other energy regions to target water. Lasers focused at many of the small peaks in infrared region of Figure 1.1 have been explored in attempts to sufficiently heat up the water in tumor cells to toxic levels. Well studied vibrational resonances in water in the microwave spectrum have also led to thermal toxicity in tumors. These techniques are successful *in vitro*, yet share the same inherent flaw: tumor cells are comprised of as much water as are healthy ones and so to radiation, normal cells and tumor cells look identical. There is no contrast in these types of therapy and so the specificity of the treatment falls entirely on the therapist's ability to focus the beam, leading to similar problems as above. The inverse relationship of absorption to penetration is the limitation of external beam therapy: if the beam can penetrate deep enough to reach non-superficial tumors, then the absorption is so low that you need a large number of photons to achieve toxic dose; if the absorption is high, then not only cant you reach deep tumors, but healthy cells along the beam path are at similar risk as the tumor.

1.2   Local LET

In principle, a better technique would be one that can somehow penetrate deep into the body and whose radiation is specifically absorbed in tumor cells only. More than simply being absorbed, the radiation needs to be lethal where it is absorbed. Relative biological effectiveness (RBE), though arbitrarily defined, is a way to compare the lethality of the same absorbed dose of two different radiation sources. In studies to find the optimum cell-killing radiation, researchers have tracked the dependence of RBE on a wide range of
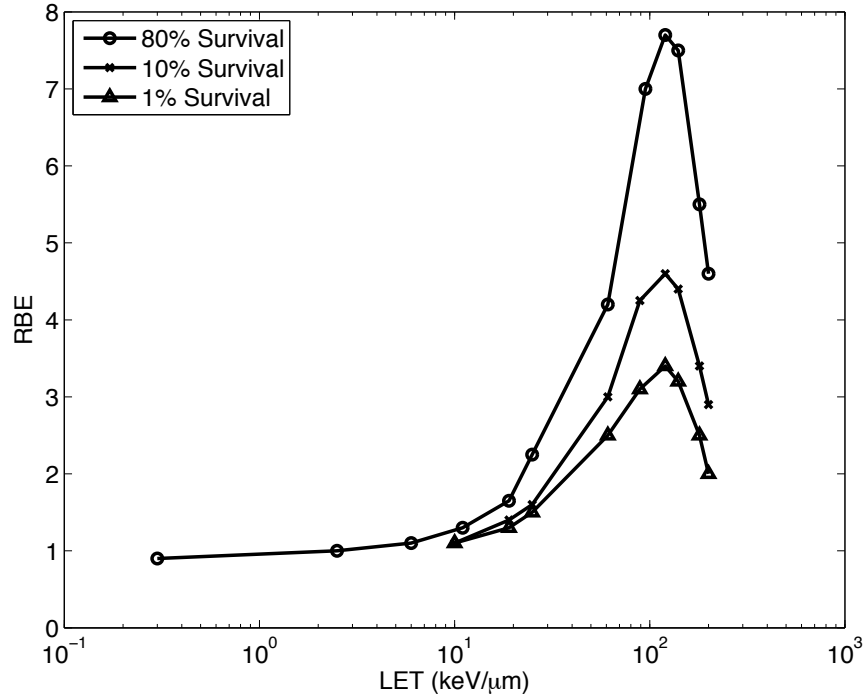
Figure 1.2: RBE vs. LET. Data re-digitized from Barendsen (1968).

variables. Perhaps the most general and informative peak is found in the dependence of RBE on linear energy transfer (LET)–the energy transferred per unit length of the track of radiation–a quantity that takes into account both the type and energy of radiation; Figure 1.2 shows this distinct peak.

LET is clearly linked with our analysis of absorption/penetration, the difference being the consideration of whether the energy lost from the particle is absorbed *locally*, or if it spawns other particles that transport the dose at a distance from the site of initial interaction. For electrons above 1 eV, the lower the energy, the higher the LET, as the lower energy particles deposit their dose in shorter ranges. This analysis holds only in the ionizing radiation energy range. Electrons, being charged particles, have the power to ionize through their entire energy spectrum, while photon ionization potential drops significant below 13.6 eV,

the binding energy of the lowest energy orbital electron in the hydrogen atom (more on the mechanisms of ionization to follow). External beams of radiation with high enough LET to be biologically destructive will not penetrate to sufficient depths without large amounts of collateral damage, but if such high-LET radiation can be made to originate within the tumor, and deliver all of its dose locally, then healthy tissue can be spared while tumor cells destroyed. While protons, α-particles, and heavier ions have increasingly higher LET because of their greater mass and charge, they have their own "red flags" ranging from higher costs to radiation safety. Electrons, however, especially low energy electrons, have LET values that approach those of heavy charged particles, and thus have higher RBEs than photons or mederate energy electrons. If a low energy electron emitter can be introduced locally to tumor cells, cell killing can be more readily controlled and more effective.

1.3 Radiobiology of Cell Killing

But what does *local* mean? In order to select the target of our radiation we must identify an efficient mechanism by which radiation kills cells. Perhaps the most efficient way to kill a cell is by double stranded breaks (dSB) in the nuclear DNA; that is, two strand breaks within ~10 bases of each other. Though there are more than 6.3×10^9 base pairs in the genome of one human cell, only one non-repairable dSB in that cell can lead to its death (Dahm-Daphi et al., 1994). This is a hugely efficient mechanism and though there are other techniques in cell killing, from thermal to pharmacological, in comparison they are akin to using the energy it takes to bash a computer to pieces with a hammer, when a simple virus changing its code can render it useless.

6

With DNA as the critical target, radiation can cause the breaks in two ways. It is possible for radiation to be absorbed by the atoms of the DNA macromolecules directly, in which case the atoms are ionized or excited, and can initiate the chain of events that leads to a break. With high-LET radiation, this "direct" process dominates because the density of ionization from this radiation is high enough so that the spacing between ionizing events is shorter than distance scale of the macromolecules. In fact, we have gotten a glimpse of this idea through the peak in RBE, which occurs at $100\,\mathrm{keV}/\mu\mathrm{m}$. In more convenient units, this translates to 100 eV/nm, which given the 2 nm diameter of the DNA double helix, means that about 200 eV is deposited as this high-LET radiation passes through the DNA. This gives a ballpark value for the amount of energy it takes to most efficiently break the bonds in DNA. This value is believable since it only takes about ~5 eV to break these bonds (UV sunlight at this energy will do enough biological damage to burn the skin) and so it makes sense that at an energy just above this, the process is most efficient.

The incident radiation, however, is not the only potential ionizer; in fact, it may not even be the most effective. If instead the radiation interacts with water, the most prevalent molecule in the cellular environment, several highly reactive products can be created; the dominant final product species are electrons and hydroxyl radicals. For example, radiation incident on water can produce an aqueous electron and an ionized water molecule. The electron often gets trapped by the polarity of two water molecules; its lifetime in this transient state is about 1 ms, which is relatively long compared to other species of products. The ionized water molecule is charged and has an unpaired electron making it both an ion and a free radical, so very unstable. This ion radical breaks up into a hydrogen ion and an hydroxyl radical, which is highly reactive having a lifetime of about 1 ns and a range of

7

about 1-2 nm in cells. This "indirect" process is thought to account for about two-thirds of all mammalian DNA damage caused by x-rays (Hall and Giaccia, 2006). What this suggests is that if a water molecule is ionized within a cylinder of about 4 nm (twice the diameter of a DNA double helix) the hydroxyl radical can diffuse to the DNA and oxidize it by extracting a hydrogen atom and leaving a radical site on the DNA. Such damage can lead to bases being altered or the sugar phosphate backbone being broken.

Still, targeting water, or even DNA, with external photons is not ideal; we have already examined the absorption issues of water and DNA's absorption peak also occurs outside the therapeutic x-ray region at 260 nm (this fact lies at the heart of spectrophotometry, which will be used in this study to verify the density of DNA in our cell line). We have seen, however, that electrons are more potent ionizers, especially low-energy ones which have short track lengths along which they deposit all of their dose. A goal for an effective cell killing mechanism would then be to produce low energy electrons whose origin (and therefore site of maximal energy deposition) is within twice the DNA helix diameter. These electrons would have the potential to ionize the DNA molecules directly, as well as the surrounding water molecules, whose resultant products can produce similar lethal lesions.

1.4   Effectively Stimulating Electrons

There are several ways in which photons can induce the emission of electrons, the most relevant to this study being the photoelectric effect. When an incident photon has energy above the binding energy of an orbital electron, the electron absorbs the photon entirely and is emitted from the atom with the energy difference between the initial photon

and the binding energy imparted as kinetic energy. This is a moderately efficient process in that for one incident photon, one electron is emitted. The resultant atom is left with an electron vacancy that will be filled by electrons from higher energy orbitals, and the process of creating and filling electron "holes" will continue until the highest energy orbital is eventually filled from the vacuum. With each electron transition, energy is conserved by either of two processes. Fluorescence is the emission of characteristic x-rays with energy equal to the difference in binding energy of the two states. The Auger process fills the same gaps by the emission of electrons; upon ejection, the kinetic energy of the Auger electron (which comes from a higher shell in the same atom) corresponds to the difference between the energy of the initial electronic transition and the binding energy for the electron shell from which the Auger electron was ejected. These Auger electrons then necessarily have lower energy than the fluorescent x-rays, because most of the energy from the initial transition is used to free the bound electron. The low energy and short range of these electrons are the sources of their potency in cell killing (see Section 4.1).

Fluorescence yields are highest for core shell (K-) electron holes, but for L- and M-shells, the Auger process strongly dominates as seen in Figure 1.3. What this means is that for atoms with $Z \geq 19$ (atoms with an M-shell), if an incident photon causes an inner-shell ionization (ISI), the subsequent emission spectrum will consist of the photoelectron, a low-energy fluorescent x-ray, and at least two low-energy Auger electrons. Also, for $Z \geq 36$ and $Z \geq 54$ atoms have an additional N- and O-shell, respectively, and though not shown in the plot, the Auger yields for these shells are nearly unity. Furthermore, if the incident photon can be tuned as closely as possible above the K-edge of the target atom, the energy of the photoelectron can be reduced. Now we can see the potential of this being a efficient
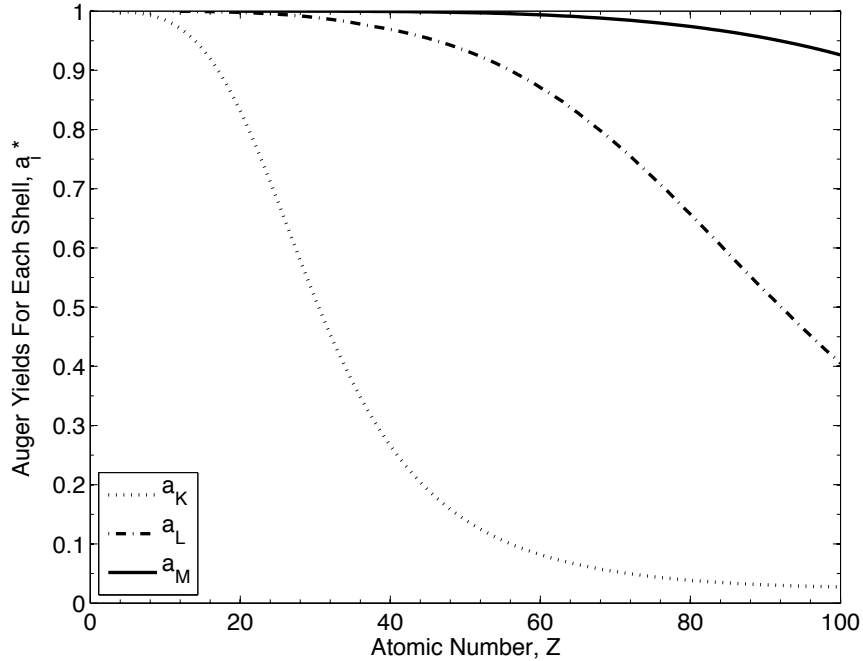
Figure 1.3: K-, L-, and M-shell Auger yields for $1 \leq Z \leq 100$. *Data are actually $(1 - \omega_i)$ where ω_i are fluorescence yields of the ith shell taken from Hubbell et al. (1994). L- and M-shell values are averages over all subshells. Coster-Kronig electrons are included, but not distinguished here.

mechanism for low energy electron yield from external radiation: one incident photon can spawn 3+ low energy, high-LET electrons as well as another low energy photon, which can spawn similar chains. Note: Coster-Kronig transitions, (the special case of Auger process in which the vacancy is filled by an electron from a higher subshell of the same shell) which are fairly prevalent in L- and higher shells, increase the number of electrons emitted during the restabilization cascade while decreasing each's energy. This process increases the number and ionizing power of the emitted electron spectrum.

Even though Auger yields are highest for lowest-Z materials, we have discussed how water is not our target; we need something to optimize contrast and the most effective target would be that which absorbs greatest in contrast to water. Figure 1.4 is a plot of the

absorption coefficient just above an elements K-edge sorted by atomic number; also plotted is its absorption relative to water. The curve decreases with heavier elements (as Compton scattering takes over as the dominant photon interaction at higher energies) despite the $\sim Z^4/E^3$ dependence since the K-edge spacing is not constant; this variability can be seen in the top axis in the figure. It should be clear that based solely on absorption, the most effective target materials would live in the range $44 \lesssim Z \lesssim 54$. The choice of target material also determines the necessary energy range of the activating radiation source; absorption has a fairly narrow peak just above the atom's K-edge, and so in order to take full advantage, the radiation source should be centered 10-15 keV above the K-edge with an energy distribution no more than 20-30 keV wide.

Thus far we have outlined two important criteria for selecting the ideal material to be used as a target in radiation-based cell killing, while simultaneously identifying the optimum energy range of the activating radiation source. Fortunately, it happens that the elements whose absorption characteristics distinguish themselves most substantially from water also lie in the range of atoms with available N-shell electrons and considerably high Auger yields. So not only will these targets stand out in the cellular environment, but once activated will mount a potent attack on the cell. Perhaps the most important issue, though, is how to get the target material into the cellular environment. This uptake can not be arbitrary, but specifically into tumor cells only, as we have argued that effective cell killing will occur wherever both the target material and activating radiation are present.
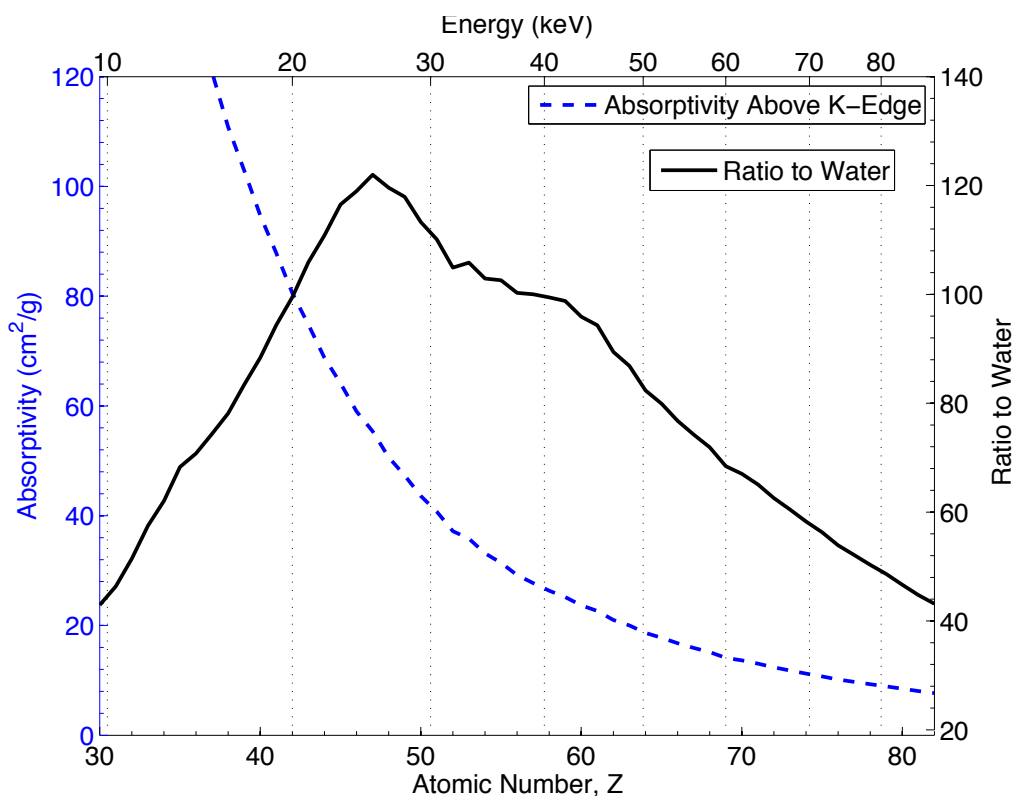
Figure 1.4: Absorption Cross Section at K-edge vs. Atomic Number, Z. Right axis is ratio of absorption coefficient just above element's K-edge to that of water at same energy.

1.5 Tumor Specificity

Perhaps the easiest and least variable method to differentiate tumors from normal cells is the length of the cell cycle. Tumor cells, for the most part, proliferate much more rapidly than do healthy cells (with some exceptions: bone marrow, intestinal endothelium). If the target material can be introduced through a process that only occurs during cell proliferation, it can lead to high tumor specificity.

During S-phase of the cell's mitotic cycle, DNA replicates itself into two identical copies. Basically, the double helix splits into individual strands, and since pairing of bases

is unique (adenine always pairs with thymidine ($A = T$) through two hydrogen bonds and cytosine always pairs with guanine ($C \equiv G$) through three bonds) each strand of the DNA carries all of the genetic information. There are several competing processes by which the cell pairs the corresponding base to the single "unzipped" DNA strand; the dominant two are through an enzyme called DNA polymerase and through *de novo* synthesis. DNA polymerase searches the existing pools of DNA bases and governs the transport of an available, suitable base to the exposed site of the DNA strand. Alternatively, a synthase enzyme can catalyze *de novo* synthesis of the necessary base, which is then used similarly to complete the pairing (more on this competition later). If a target material can be attached to or disguised as one of the DNA bases and enough of it introduced into the intracellular pools, then it would be plausible to selectively incorporate the target material into nuclear DNA of only tumor cells.

1.6   The Solution

This tumor-avid uptake, along with an enhanced absorption contrast to water and a robust electron emission spectrum, constitutes the criteria for optimum radiosensitizer; iododeoxyuridine (IUdR) meets all three standards. Iodine, as well as the rest of the halogens, just so happen to "look" like a methyl group in a chemical sense. Like the methyl group, halogens are one electron short of stability and have van der Waal's radii of approximately 200 pm (Prusoff et al., 1979). As such, the halogens can be substituted for the methyl group in the DNA base thymidine to make up what are called halogenated pyrimidine analogues. The chemical structure is so similar that these analogues are nearly indistinguishable to the

cell and will populate the thymidine pools from which DNA polymerase searches when there is an unpaired adenine during DNA replication; this process is called the thymidine salvage pathway. Of the halogens, iodine is not only closest in size to the methyl group and so should be maximally incorporated, but is also the only one that lives in the optimum target range discussed above (Z=53, K-edge @ 33.2 keV).

Besides the microbiological highlights, there are several other factors that classify the use of IUdR as advantageous. If successfully substituted in the DNA, IUdR is biologically stable. In the human body, iodine that is not taken up in the DNA is directed to the thyroid gland, and then eventually excreted with biological half-lives reported from to be on the order of minutes to hours (O'Farrel and Dunuaway, 1969; Semnani et al., 2005). Administration of IUdR days before radiation treatment will ensure that non-substituted iodine will not linger. This isolation dilemma is one of the most important hindering the use of radioactive iodine in a similar fashion. Studies have shown extreme efficacy of cell killing in tumors through [125]IUdR therapy(Faraggi et al., 1994; Commerford et al., 1980; van Dieren et al., 1996), but others have also tracked the dose to the liver as the non-substituted iodine leaves the body (Kinsella et al., 1994). In fact, radioactive IUdR is used as a proliferation tracer of tumors in the liver. Since iodine builds up in the liver, the dose of radiation coming from the [125]IUdR is used to monitor the rate of cell proliferation. Using externally initiated radiation with stable iodine allows the therapy to be isolated where only the substitution in the region of irradiation is toxic.

It is clear from Figure 1.4 that if it is feasible to operate at lower photon energies, radiosensitizing materials like iodine would be more efficiently absorbed in cells than higher-Z materials, regardless of sensitizing mechanism. This idea has been discarded in the past

14

because of the inadequacies of external beams of such low energy. Almost all the dose from low energy photons is deposited at the interaction site and so external, low energy beams fail to treat non-superficial tumors without doing much collateral damage along the beam path. Also, chemotherapeutic and radiosensitizing drugs containing platinum (Z=78, K-edge @78.4 keV), for example, have shown some promise in the clinic. Still, these have be combined with megavoltage x-rays and so lack an efficient absorption mechanism. If, however, the more efficiently absorbed, low energy x-rays were administered from within, as in brachytherapy, this synergy of enhanced absorption contrast and tumor specificity can be taken advantage of.

1.7   Brachytherapy and its Past Inadequacies in Combination Therapy

Brachytherapy involves implanting radioactive material in the body with close proximity to the tumor. Medical physicists have written and implemented robust treatment planning software to account for heterogeneous tissue, attenuation, and anisotropic dose delivery, so treatment of lesions ranging from minuscule metastases to golf-ball-sized tumors have been well developed. Manual localization of the radiation source ensures consistency of treatment distance, predictability of dose distribution, and perhaps most importantly, the tumor can be treated with a high dose of radiation, while reducing the probability of damage to healthy tissue. For instance, it is potentially harmful to irradiate the lung, but using external beam therapy to target the pancreas, it is difficult to achieve significant dose with one beam without substantial damage along the beam path and even more difficult to use distinct beams without one of them bypassing a lung. For this reason, along with the

Table 1.1: Common Brachytherapy Materials

Radionuclide	Half-life	Photon Energy (MeV)	Exposure rate constant $\Gamma(\frac{R\,cm^2}{mCi\cdot hr})$
^{226}Ra	1600 yr	0.047-2.45 (0.83 avg)	8.25
^{222}Rn	3.83 days	0.047-2.45 (0.83 avg)	10.15
^{60}Co	5.26 yr	1.17, 1.33	13.07
^{137}Cs	30.0 yr	0.662	3.26
^{192}Ir	73.8 days	0.136-1.06 (0.38 avg)	4.69
^{198}Au	2.7 days	0.412	2.38
^{125}I	59.4 days	.028 avg	1.46
^{103}Pd	17.0 days	.021 avg	1.48

convenience of outpatient procedures, brachytherapy patients often have lower risks of the adverse side effect associated with radiation therapy.

Common seed materials for brachytherapy are listed in Table 1.1, along with their half-lives and average energy. Notice how the common radioisotopes fall into two basic categories: low and high energy. Herein lies the clue to their ineffectiveness in combination therapy. The higher energy seeds have a larger penetration depth and can therefore deliver dose to larger tumors. The thing to note, however, is that above about 80 keV, more that 92% of photon interactions in water are Compton scattering processes where much less energy is transferred, and so full absorption is not localized to the site of the initial interaction. Photoelectric absorption accounts for less than 3% of interactions (but 21% of the energy transferred) at 80 keV and this percentage falls dramatically over 200 keV to 0.1% of the interactions (and 1% of the energy transferred) (Johns and Cunningham, 1983). It is clear that higher energy photons, although having their benefits, do not take advantage of any efficient absorption mechanism and therefore are not ideal for targeting radiosensitizers. The low energy seeds take advantage of the relatively high absorption and are effective as a stand alone therapy for small tumors Sloboda (2003); Sharkey et al. (2002). Notice,

however, that both ^{125}I and ^{103}Pd emit the majority of their radiation below the 33 keV K-edge of iodine and so again do not take full advantage of this photo-absorptive contrast. This explains their inefficiency in combination therapy despite their relative effectiveness as stand alone radiation sources. It should be clear that a low energy photon source, just above the K-edge of iodine would take advantage of the iodine photo-absorption, the absorptivity contrast relative to water, and the fact that 80% of the total energy transferred to water at this energy is done through photoelectric processes.

Interest in low energy brachytherapy has increased over the last decade and people have began to develop different ways to make these low-energy x-rays. An alternate technique that has been getting more attention is implantable x-ray tubes. The so-called "electronic brachytherapy" consists of a miniature x-ray tube the size of a resistor connected to a portable controller that can adjust the operating voltage up to 50 kVp and therefore change the dosimetric properties of the therapy. Much work has been put into doing a dosimetric characterization of these mini tubes, but their use remains experimental (Beatty et al., 1996; Gutman et al., 2004; Liu et al., 2008). Alternatively, synchrotrons and Compton backscattering accelerators are able to provide clean x-ray beams at this energy with sufficient flux to be useful. Though much research has been done using these tunable beamlines to find the optimum activation energy for IUdR (Corde et al., 2004), these existing sources of monochromatic x-rays at this energy are prohibitively expensive and geographically sparse, and so support for this theoretically efficient combination has been abandoned for practical reasons. Search for a useful activation source led us to nuclear physics.

1.8   Narrowing the Search

The prime candidate for a brachytherapy material, given IUdR as the target, is a narrow band x-ray source with photon energy centered at 50 keV, above the 33 keV K-edge of iodine at the peak of the absorption contrast relative to water (see Figure 4.1). With that in mind a search of the entire periodic table can be narrowed substantially. This photon energy lies in the x-ray region, and more specifically the K-x-rays (even the heaviest elements feasibly produced have L-edges below iodine's K-edge). These x-rays come from atomic transitions, but can be produced after nuclear decay. The relevant process is electron capture (EC) where an inner-shell electron is absorbed by the nucleus. The electron combines with a proton to form a neutron and an energetic neutrino. Since the number of protons decreases by one while the number of neutrons increases by one, the resultant nuclide is different from the original, but the atomic mass number remains unchanged. The subsequent atom is now in an excited state with an inner-shell electron vacancy, and will restabilize itself through fluorescence or the Auger process as discussed earlier. Recall that fluorescence dominates at higher-Z (elements whose K-edge is high enough to generate characteristic K-x-rays in our target energy range) and so as the electron hole is filled, narrow band x-rays will follow. Other possible outcomes of EC decay are the population of excited nuclear states of the resultant nuclide or even ground states of unstable nuclides that will undergo subsequent decay. The criteria for our search is then limited to nuclides 1) who undergo EC only (with no probability of $\alpha-$or $\beta-$ decay since these lead to other radiation absorption mechanisms that could be detrimental to healthy cells with no IUdR incorporation), 2) that decay mainly into the nuclear ground state of a stable daughter nu-

clide (eliminating high-energy γ−rays from excited nuclear state transitions), 3) whose characteristic K-x-rays fall between 40-60 keV, and 4) that decay with a relatively short half-life. Brachytherapy treatment plans often call for low dose fractions and so to limit the handling dose to personnel and require much less strict removal times, it is beneficial to have the source decay completely while implanted. Also, long-lived radioactive materials have a list of safety concerns unto themselves. Despite the vast number of available nuclides in this energy range (NNDC, 2009), only one nuclide fits all the criteria. ^{161}Ho is a pure electron capture agent that decays mainly into the nuclear ground state of ^{161}Dy; excited nuclear states of dysprosium are very rarely populated. With a 2.54 hour half-life, the decay produces atomically excited states of dysprosium with an inner-shell electron vacancy. As the atom restabilizes, the electrons reorganize to fill this hole, and the dysprosium atom emits its characteristic x-rays ($K_{\alpha,\beta}$ @ 45 and 52 keV, respectively). The low energy L- and M- x-rays are easily filtered out, and so the spectrum consists principally of K x-rays, free of long-lived or beta-decaying isotopes.

The goals for this project were twofold: first, to create, characterize, and measure the amount of holmium we were able to produce; and second, to carry out *in vitro* studies to determine if this combination of radiosensitizer and x-ray source was, in fact, more effective in cell killing than other treatment modalities. Before the second goal was accomplished though, there was a need to develop the analytical machinery to define what "effective" meant, and which mechanisms of dose enhancement and sensitization led to cell killing.

19

CHAPTER II

CREATING AND MEASURING RADIOACTIVE HOLMIUM

In this study, we created radioactive holmium via proton bombardment of dysprosium, measured the production yields, and assessed the therapeutic potential of the subsequent narrow-band x-rays.

The dysprosium foil target consisted of a 3 mm square cut from a 25 mm x 25 mm, 0.1 mm thick, 99.9% (REO) sheet (Alfa Aesar, USA). The foil was placed in a graphite target holder made from a 3/8in x 6in cylindrical AXF-5Q graphite rod of density 1.78 g/cc (Poco Graphite Inc., USA). The graphite rod is highly pure with the largest contaminant being Ni at a concentration of 0.01 parts per million. The target holder was fabricated into a cap with a 1.5 mm diameter hole in the face to reveal the foil as seen in Figure 2.1; the cap threads onto the support to put the foil in thermal contact with the graphite. The entire apparatus was then placed in a water cooled aluminum Faraday cup and attached to the line 1 of the VUMC RDS 112 cyclotron. The bombardment was performed at approximately 10 μA of proton beam current for 10 seconds (exact charge integration will follow in Section 2.1). Following irradiation, the activity measurements were carried out by γ-ray spectrometry using a calibrated GMX 35P4 high purity germanium (HPGe) coaxial detector (EG&G Ortec, USA) and the Gamma Vision acquisition system (Version 6.01, EG&G Ortec, USA). An Isotope Products multi-nuclide standard check source (Eckert & Ziegler AG, Berlin, Germany) with detector geometry identical to our experiment was used to produce a point-source efficiency calibration curve.
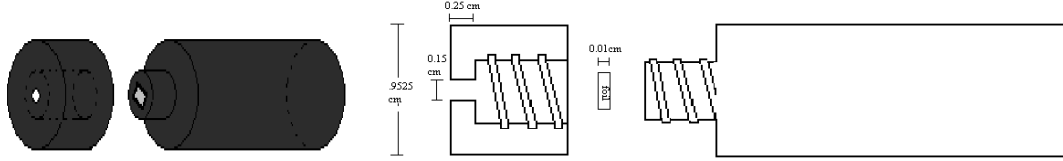
Figure 2.1: Target holder assembly: 3-D depiction and 2-D cross section. The beam axis runs from left to right.

2.1   Activity Calculation

The foil was placed in the HPGe detector and counted 41 times consecutively. To decrease dead time, the foil was fixed approximately 25 cm from the germanium crystal. For each run, the GAM32 analysis engine produced the background counts and net area counts for each peak at its centroid energy as well as the percent uncertainty of these counts. With these data for each run, the net area counts per second (corrected for dead time) were plotted versus time for each peak and the curves fitted as a decaying exponential using the fitting toolkit from pythonlabtools, available online(Mendenhall, 2008).

Charge Calibration

The cyclotron is not equipped with an accurate beam current integrator; to calculate production data from the activity yields, we performed a charge calibration. The total number of incident protons and the exact energy of each cannot be replicated precisely by additional experiment and so the calibration must be performed concurrently with the irradiation of the foil. To accomplish this, we used the graphite target holder as our reference. At a proton energy of 11 MeV, the reaction $^{12}C(p, \gamma)^{13}N$ yields ^{13}N at a rate of $250 \frac{MBq}{\mu A\,hr}$(Krasnov et al., 1969) or in more useful units, $Y_C = 6.9 \times 10^4 \frac{MBq}{C}$. Assuming a reasonably uniform beam, the ratio of the charge incident on the dysprosium foil to that incident on the cap,

21

$Q_{\mathrm{Dy}}/Q_{\mathrm{C}}$, is equal to the ratio of the area of the exposed foil to the area of the exposed carbon (graphite). The stopping range of protons in graphite is $\lambda = \int (\frac{dE}{dx})^{-1} dE = 0.78$ mm (Berger et al., 2008). Notice from Figure 2.1 that this penetration depth is less than 2.5 mm, the thickness of the portion of the cap that covers the foil. Thus, protons that did not travel through the hole in the cap did not reach the foil and could therefore not contribute to any production. The cross-sectional area of the foil irradiated is then the area of the hole in the cap, so $A_{\mathrm{Dy}} = A_{\mathrm{hole}} = 0.018\, cm^2$. The area of the exposed graphite cannot be observed directly, but instead we can observe the ratio of its area to the area of the hole. To accomplish this, we performed a control experiment in which we used a small graphite sheet in place of the dysprosium foil in our same graphite target holder; since the production yield is the same for the graphite cap and sheet, the ratio of activities will equal the ratio of the areas exposed to the proton beam. This ratio was observed to be $\gamma = \frac{Act_{\mathrm{cap}}}{Act_{sheet}} = \frac{A_{\mathrm{beam}}}{A_{\mathrm{hole}}} = \frac{Q_{\mathrm{C}}}{Q_{\mathrm{Dy}}} = 18.8$; the incident beam cross-section is then $A_{beam} = 0.33\, cm^2$. The yield calculation for each isotope, ^{i}Ho, of holmium is then summarized as follows.

$$Y_{\mathrm{Dy} \to ^i\mathrm{Ho}} = Y_{^{12}\mathrm{C} \to ^{13}\mathrm{N}} \frac{Act_{^i\mathrm{Ho} \to \mathrm{Dy}}}{Act_{^{13}\mathrm{N} \to ^{12}\mathrm{C}}} \cdot \gamma$$

Subtleties of Graphite Activity Measurement

Since ^{13}N has a half-life of 9.965 minutes, it was important to start measuring the graphite cap immediately after bombardment in order to accurately count the short lived 511 keV annihilation peak. The HPGe detector would saturate and dead time would become unmanageable with such a "hot" sample so shortly after being irradiated. To circumvent this problem, we used a Victoreen 450 Ionization Chamber (Elimpex-Medizintechnik,

Austria) to measure the exposure rate of the cap. We observed the exposure rate every 60 seconds from 6 minutes after bombardment to 68 minutes after bombardment; data were subsequently converted from exposure to activity ($\Gamma = 0.0407 \frac{\text{C} \cdot \text{cm}^2}{\text{kg} \cdot \text{GBq} \cdot \text{hr}}$ ($5.84 \frac{\text{R} \cdot \text{cm}^2}{\text{mCi} \cdot \text{hr}}$) for ^{13}N in air). The internal geometry of the ion chamber, however, is complicated and the final reading is an integral over all angles in which photons pass through the pressurized gas chamber along with the rate at which these energy photons create ion pairs. The graphite cap was placed close enough to get sufficient signal, but being so close, the results are biased by the geometrical uncertainties in the $1/r^2$ point source and detector approximation.

To correct for this geometry problem we performed another control experiment. An ^{18}F sample from the Vanderbilt University Radiopharmacy(PETNET Pharmaceuticals Inc., 2002) (produced daily and used for PET scans), was standardized in a dose calibrator that directly reports the activity (in mCi) of a given sample of ^{18}F. This particular isotope of fluorine is a pure 511 keV source (positron emitter) with a half-life of 109.7 minutes. We duplicated our previous geometry with the ion chamber and by measuring the exposure rate, given the observed activity ($\Gamma = 0.0418 \frac{\text{C} \cdot \text{cm}^2}{\text{kg} \cdot \text{GBq} \cdot \text{hr}}$ ($6.0 \frac{\text{R} \cdot \text{cm}^2}{\text{mCi} \cdot \text{hr}}$) for ^{18}F in air), we can determine r, the effective distance from the source to the detector. ^{18}F activity was reverified at the end of the experiment to confirm charted decay constant.

After 88 minutes (about 9 half-lives of the decaying ^{13}N) from bombardment, the cap was counted in the HPGe detector for 20 consecutive 60-second runs. These data were then fitted and compared to the ion chamber data for corroboration.
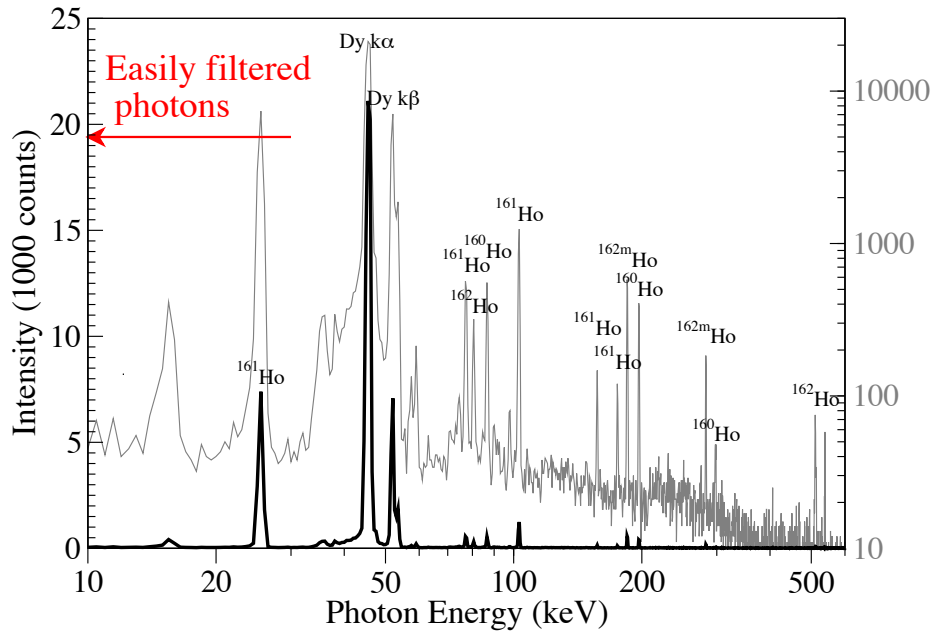
Figure 2.2: Photon spectrum for proton irradiated dysprosium: Bold plot corresponds to left (linear) axis. Gray plot corresponds to right (logarithmic) axis.

2.2   Spectroscopic and Dosimetric Characterization

Spectroscopy

The spectrum generated by the detector software for the first of the 41 total counts on the foil is displayed in Figure 2.2. As can be seen, we have created a clean spectrum with strong peaks at 45 and 55 keV, and very little activity anywhere else in the spectrum. Isotopes created were identified to be ^{160}Ho, ^{161}Ho, and two nuclear states of ^{162}Ho, all of which decay by electron capture (the excited state of ^{162}Ho decays partially by internal transitions, see Section 2.2). Since photons emitted in EC depend on atomic structure, and not nuclear structure, neighboring isotopes of the same element emit identical x-ray photons. Thus, identification of photon energy is not enough to ensure that any particular line in our spectrum does in fact correspond to a specific initial isotope; the decay of these peaks over time must also match the half-lives of the appropriate isotope.

^{161}Ho decay

Gamma ray matching (both energy and decay rate) is the key to proper isotope identi-
fication for a mixed source. Consider the 25.4 keV peak associated with the ^{161}Ho decay
depicted as set (2) in Figure 2.3. The data fit well to gamma emission produced from the de-
cay of an isotope with 149.6 minute half-life; ^{161}Ho has a half-life of 148.8 minutes. Other
than the K- and L- x-rays that come from the EC decay, there are only two other notable
peaks, one at 77 keV and the other at 103 keV ((11) in Figure 2.3); each fit equally as well
to the 2.5 hour half-life, and their individual abundances match the intensity differences in
the branching ratios.

^{162}Ho decay

The 185 keV peak shows good evidence for the existence of the excited state of ^{162}Ho,
^{162m}Ho, which decays by EC (38% probable) back into the ground state of ^{162}Dy with a
half-life of 67 minutes. Set 5 of Figure 2.3 illustrate this decay. Again, not only do we have
the other notable peaks in the decay, (namely 282, 937, and 1220 keV) but they all fit well
to the 67 minute half-lived exponential. The 511 keV annihilation peak is evidence of the
other decay chain of ^{162}Ho. Curve (10) of Figure 2.3 fits well to a half-life of 67 minutes
running parallel to data for the 185 keV peak (set (5)). This radiation, however, is created
in the ground state decay of ^{162}Ho back to ^{162}Dy, which has a 15 minute half life, but it
is populated from the 67-minute IT decay of ^{162m}Ho (62% probable) that fills the ^{162}Ho
ground state. Recall that in a decay series where the parent isotope is longer lived than its
daughter, a transient equilibrium will be reached in which the behavior of the decay series
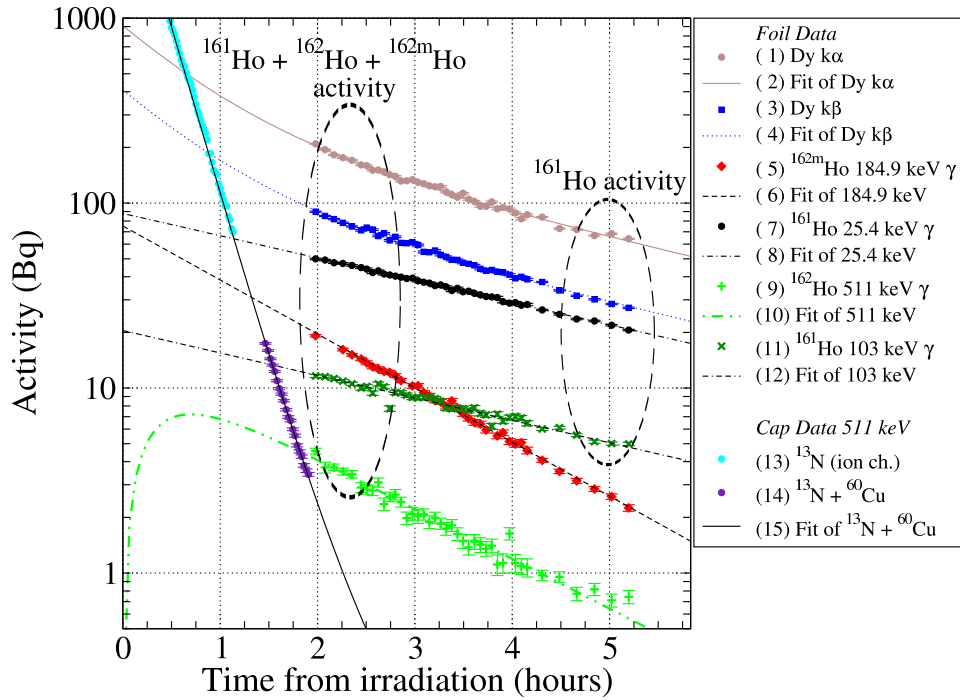
Figure 2.3: Key Decay Curves. Plotted are the background subtracted, dead-time corrected, net areas (in counts/sec) ±1-sigma for each of the 41 counts in the detector versus time for several key peaks. The decaying exponential fits were generated by the modified Levenburg-Marquardt (L-M) algorithm consisting of 50 L-M steps with the decay constant parameter frozen followed by a single step with the decay constant as a free parameter which produces a nonzero covariance matrix that substantiates the reduced chi-squared value.

will mimic the half-life of the longer lived parent isotope. The 1330 keV peak exhibits the same behavior; this along with the 38 keV peak that comes directly from the IT decay are substantial indicators that we are in fact populating both the excited and ground states of ^{162}Ho, and that both branches in the decay scheme of the excited state are active.

^{160}Ho decay

The decay data corresponding to the creation of ^{160}Ho are noisy, due to low yield, with relatively high uncertainty. The activity has a longer decay constant (5.02 hour half-life)

26

on the fringe of our detection ability in this experiment. We do, however, see a sufficient number of ^{160}Ho lines to have high confidence in its identification. Very few high energy gammas are produced in the IT decay into the ground state (65% probably), while similar dysprosium K x-rays are emitted during the EC decay (35% probable).

X-rays

The K- x-rays are at the heart of this paper, yet their time dependence is not a single exponential, making it hard to compute nuclear yields from them. This can be easily understood when the origins of these photons are considered. ^{160}Ho , ^{161}Ho , as well as the ground state and one branch of the excited state of ^{162}Ho decay by EC which leaves a K-shell hole in dysprosium; the atom stabilizes by photoemission of these K- x-rays. Accordingly, there are four different sources of photons with the same energy in our system, each of which decays at a different rate, ranging from 15 minutes to 5 hours. The majority of the activity comes from the two holmium isotopes, ^{162m}Ho and ^{161}Ho, and so the data fit fairly well to a sum of exponentials, one with 67 minute half-life and one with 149 minute half-life; the curves (2) and (4) (running through sets (1) and (3)) of Figure 2.3 show these 2-component fits. With the counting statistics available, we cannot meaningfully fit a sum of four exponentials (8 free parameters) on only 41 data points, so we present our data as shown. Since the short-lived component decays too quickly to be relevant for applications, and the long-lived one has too low activity to be germane, their omission is inconsequential to the results, but account for the slight imprecision in the fit.

Charge Calibration

The exposure rate of the graphite cap was recorded every 60 seconds for 62 minutes and the results are plotted as set (13) in Figure 2.3. The half-life of 10.3 minutes can be easily identified as the β^+ decay of ^{13}N into ^{12}C. Immediately after measuring the cap with the ion chamber, it was brought to the HPGe detector and counted as described above; the energy of the nitrogen decay was confirmed as annihilation radiation. The spectrum of the cap in the detector revealed only one contaminant, ^{60}Cu, probably originating from the trace amount of Ni present in the natural carbon. The ^{60}Cu decay, consisting of three higher energy gammas (826, 1332, and 1790 keV) along with a 511 keV annihilation peak, are easily identified and fitted to the 23.7 minute half-life. ^{11}C, a pure positron emitter having a 20.4 minute half-life could also have been created by the plausible (p, pn) reaction, but would be indistinguishable from the ^{60}Cu decay. We fit the annihilation peak data to a double exponential to pick out the two half-lives. Set (14) in Figure 2.3 shows the detector data and curve (15) connecting both cap data (ion chamber and detector) is the fit to a sum of decaying exponentials, one with the 9.965 minute half-life of ^{13}N, the other with the 23.7 minute half-life of ^{60}Cu. Once corrected for efficiency and branching ratios the fit yields 11.36 MBq of ^{13}N. From this we find the incident charge on the cap $Q_\mathrm{C} = 160\,\mu C$.

Production Yields

Results for the key peaks are tabulated in Table 2.1. Some of the peaks come from two different isotopes or different nuclear states of the same isotopes; for this reason, not every value for total nuclei of the same isotope created matches. What we can see however, are

Table 2.1: Total production for the key peaks in the spectrum. Isotopes listed identify which branching ratio was used in calculation. Note that the yields are not weighted by the isotopic composition of natural dysprosium because we can not differentiate the production channels of each isotope.

E_γ(keV)	Ho isotope	Peak Activity $\pm 1\sigma$ (kBq)	# Nuclei ($\times 10^8$)	Yield (GBq/C)
25.41	161	$70.8 \pm .5$	9.2	8.2
45.21	161	$120.1 \pm .7$	†	14
45.99	161	$59.5 \pm .4$	†	6.9
52.11	161	$139.1 \pm .9$	†	16
80.7	162	94.4 ± 2.2	4.9	11
86.49	160	$1.61 \pm .05$	0.41	0.19
103.04	161	$59.8 \pm .9$	7.8	6.9
184.85	162	$29.5 \pm .4$	1.7	3.4
196.88	160	$1.21 \pm .05$	0.31	0.14
282.84	162	$31.6 \pm .6$	1.8	3.7
511.17	162	54.0 ± 2.3	3.2	6.2
728.3	160	$1.37 \pm .06$	0.36	0.16
937.29	162	$40.1 \pm .2$	2.3	4.6
1220.1	162	42.6 ± 1.1	2.3	4.9
1312.6	162	$24.9 \pm .2$	1.4	2.9

† For the x-rays, the 148.8 minute half-life component has been separated in the double exponential fit and used to isolate the ^{161}Ho, but the multiple origins of these photons renders the calculated number of nuclei created inaccurate.

the matching peaks corresponding to the same decay chains. Notice, for example that the 184, 282, 937, and 1220 keV peaks, which all come from the 67- minute decay of ^{162m}Ho into the ground state of ^{162}Dy, all have similar values for the total number of nuclei created, a weighted average of approximately 2.2×10^8 nuclei of ^{162m}Ho. Also, the 25 and 103 keV peaks, which come from the 2.48 hour decay of ^{161}Ho into ^{161}Dy, both count the similar number of ^{161}Ho nuclei created, the weighted average being 8.8×10^8 nuclei. The 80.7, 511, and 1320 keV peaks illustrate the 15-minute ground state decay of ^{162}Ho into ^{162}Dy. There are several sources of error in these numbers. First, the 80.7 keV peak comes from the decay of both the excited state and ground state of ^{162}Ho and so there are two decay

constants and two branching ratios that are not separated out in this table. We may have also populated the ground state directly at bombardment, so the true origins of these three peaks cannot be accurately determined, which is why their activity does not serve to precisely estimate the number of nuclei created. The important things to take from these data are the orders of magnitude involved. We have made approximately four times more ^{161}Ho than the ground and excited states combined of ^{162}Ho and a factor of 24 more ^{161}Ho nuclei than ^{160}Ho, the longest lived contaminant (3.6×10^7 nuclei). Furthermore, even though there are some higher energy gammas coming from the ^{160}Ho decay at the percent level, this decay contributes even more of the same, low-energy x-rays. So too does the decay of ^{162}Ho, which because of the shorter half-life is even less detrimental as a contaminant. For analytical purposes we use the individual gamma rays as a standard to see the total number of each isotope created, but for applications, the amount of high energy contamination is overshadowed by the significantly higher number of useful, low-energy x-rays.

An important note on error analysis: as you can see from the activity error bars (which consist of propagating the detector's counting statistics and the fitter's Poisson statistics) we have clean, distinct peaks that fit very well to decaying exponentials. The values calculated from these activities, such as nuclei created, and production yield, all depend on the carbon-nitrogen yield found in Krasnov et al. (1969). In this paper, Krasnov quotes the "total error of the resulting isotope yield values was $\pm 10\%$", which if were correct, would propagate through and dominate the small statistical error, and so all further calculated values would have 10% error.

Reaction Channels

The work presented here does not contain sufficient information to uniquely identify the nuclear processes that yield the various nuclides. However, it is possible to make some general considerations which can suggest possible improvements to the yield based on the isotopic composition of the parent material.

We have carried out nuclear modeling using the CEM03 nuclear physics code (Mashnik and Sierk, 2002). This code is primarily intended for protons above 100 MeV, but discussion with its authors has led us to believe that it is still reasonable at much lower energies. These calculations have shown that (p,n) and (p,2n) reactions are likely, with (p,n) being the dominant channel. Accordingly, ^{161}Dy is probably the most important parent isotope, and since it is only 19% abundant in natural dysprosium, one could improve the yield significantly by starting with enriched material. That being said, even with the natural dysprosium foil, we have generated plenty of x-rays to use therapeutically and very few contaminants, making this technique cost efficient and practical.

Therapeutic Relevance

The air kerma rate constant for ^{161}Ho in SI units is $19.9 \frac{\text{cGy} \cdot \text{cm}^2}{\text{GBq} \cdot \text{hr}}$ ($0.74 \frac{\text{cGy} \cdot \text{cm}^2}{\text{mCi} \cdot \text{hr}}$). Rates for the other isotopes produced can be calculated similarly, but since the spectrum is dominated by ^{161}Ho and the gamma intensity produced in the ^{162}Ho decay will decline substantially during transport to a patient, this is the most predictive measure of the dose deposition. Given a proton energy of 11.6 MeV and a beam current of $50 \mu A$ we can produce ^{161}Ho at a rate of $0.023 \frac{\text{GBq}}{\text{min}}$ ($0.61 \frac{\text{mCi}}{\text{min}}$). It is important to note that the holmium will decay during

Table 2.2: Dosimetric profile and modestly estimated production capabilities of ^{161}Ho. Values are compared to commercially available model 6711, ^{125}I Oncoseeds.

Nuclide	Air Kerma Rate Constant $\Gamma(\frac{cGy \cdot cm^2}{GBq \cdot hr})$	Production Rate $\left(\frac{GBq}{min}\right)$	Available Activity (GBq)	Initial Dose Rate @ 0.5 cm $\left(\frac{cGy}{hr}\right)$	Integrated Dose @ 0.5 cm after 12 hours[b] (cGy)
^{161}Ho	19.9	0.023	1.8[a]	148	540
^{125}I	35.7	-	≤0.37 per seed	53	640

[a]Activity produced after 3.6 hour bombardment at $50\,\mu A$.
[b]96.5% decay of a 2.48 hour half-life source will occur after approximately 12 hours or overnight.

longer irradiations so for irradiations longer than the mean lifetime of the isotope (3.6 hours for ^{161}Ho) production will saturate. After 3.6 hours, then, we can make 1.8 GBq (48.7 mCi), which at a treatment distance of 0.5 cm will deliver 540 cGy of air dose. For comparison, we have included similar calculations for model 6711, ^{125}I Oncoseeds (Oncura Inc., Plymouth Meeting, PA).

2.3   Engineering Advances

Important to keep in mind are the equipment and facilities used in this study relative to the state-of-the-art. Figure 2.5 depicts the evolution of our target holder designs. The first generation (schematics of which are pictured in Figure 2.1) was designed for very low current and beam time. This was the apparatus used in the spectroscopic characterization of the radiation induced during bombardment. The graphite was sufficient in dealing with the minimal amounts of heat during these short (~10 second) cyclotron runs and also provided the useful framework for the charge calibration as discussed in Section 5.5.

The second generation introduced some water cooling to withstand longer bombardments. In consisted of a copper core through which chilled water circulated, carrying heat away from the foil. The foil was situated on the flat tip of the copper rod and fastened in place by a graphite cap that threads onto the copper. The aluminum shell simply couples the entire apparatus to the cyclotron and sustains the vacuum level. Several graphite caps were experimented with to optimize beam transmission, structural integrity, and heat control; the "pepper shaker" design was used most frequently because of the ease in handling and the condition of the foil upon extraction after its use.

For *in vitro* irradiations, the third generation target assembly was designed and implemented. Since much longer and higher-current bombardments were necessary to deliver sufficient activity, and therefore dose to cells, the cooling system needed to be improved to allow for full beam transmission with no foil degradation for several hours. This generation combined water- and helium-cooling. The front (beam-in) face of the target assembly is solid with a hole along the beam axis one centimeter in diameter (more than twice the ~4 mm beam diameter) that exposes the front face of the foil, both sides of which were covered and baked in silicone to ensure complete vacuum seal and prohibit any contamination. There is a rubber O-ring that sits in an etching on the back side of the front face which keeps a vacuum seal between the foil and this face. In fact, the foil acts as the window and keeps an air-tight seal from the front face to anything farther down the beamline. This is crucial since the back of the foil is to be cooled by a constant flow of helium, which is a fairly inert gas, but which could still cause damage to the cyclotron if this seal were broken (actually when the vacuum is lost (pressure $\gtrsim 1$ mPa), one of the many safeguards of the cyclotron is automatically activated and the machine is immediately shut down).

The helium is pumped through a thick washer that has a small passage bored out perpendicular to the beam axis. The holes in the washer are aligned with the pathways in the outer brass housing so that the helium flows through to the opening in the middle disk. This opening is sandwiched air-tight between the back face of the foil and the front face of the water-cooled, aluminum backing that is fastened in thermal contact to the middle disk. Chilled water is circulated through the aluminum back, which in turn cools the disk. Since the center of the disk is cut out (the same diameter as the front hole), virtually none of the beam's energy is deposited in it, and so it remains chilled and serves to cool the helium even further as it flows. The chilled middle disk also serves to cool the part of the foil not exposed to the beam through the front hole.

We used a thin (100 micron) foil since the stopping range of protons at this energy is about 400 microns. The production cross section decreases substantially as proton energy decreases and so after the first 100 microns, the beam would probably do more to heat the foil than increase the production yield.

As an estimate, we performed a Coulomb-apsis calculation to determine the approximate energy dependence of the production cross section. At an energy of 11.6 MeV, assuming a reasonable cross section (the average value from the Shen, Tripathi, and Tripathi (light reactions) calculations of the total reaction cross section is $\sigma \approx 340\,\mathrm{mb}$ (Tripathi et al., 1997, 1999; Shen et al., 1989)) we can calculate the distance of closest approach of the proton to a dysprosium ($Z = 66$) nucleus considering only Coulomb repulsion. Let the distance of closest approach be r_{min} and the corresponding speed of the proton be v_{min}.

Conservation of energy (neglecting nuclear recoil) yields,

$$E = \frac{1}{2}mv_{min}^2 + \frac{Z_1 Z_2 ke^2}{r_{min}}. \tag{2.1}$$

Conservation of angular momentum relates the impact parameter b to r_{min}:

$$mvb = mv_{min}r_{min}. \tag{2.2}$$

The kinetic energy of the proton then becomes

$$E = \frac{1}{2}m\left(\frac{vb}{r_{min}}\right)^2 + \frac{Z_1 Z_2 ke^2}{r_{min}}. \tag{2.3}$$

The solution for r_{min} is

$$r_{min} = \frac{\alpha}{2E} + \sqrt{\frac{\alpha^2}{4E^2} + b^2} \tag{2.4}$$

where $\alpha = Z_1 Z_2 ke^2 = 66 \times 1.44\,\mathrm{MeV\,fm}$ and $\sigma = \pi b^2$. Inverting this relation we solve for b and ultimately the cross section, σ, as a function of E with our calculated r_{min} as a constant.

$$\sigma(E) = \pi b^2 = \pi\left(r_{min}^2 - \frac{\alpha r_{min}}{E}\right) \tag{2.5}$$

The results of Equation 2.4 yielded $r_{min} = 9.35\,\mathrm{fm}$. The more detailed calculations of Tripathi et al. (1997, 1999); Shen et al. (1989) , which include geometrical and charge screening corrections, agree on a slightly different result (i.e. $r_{min} = 9.68\,\mathrm{fm}$) for the
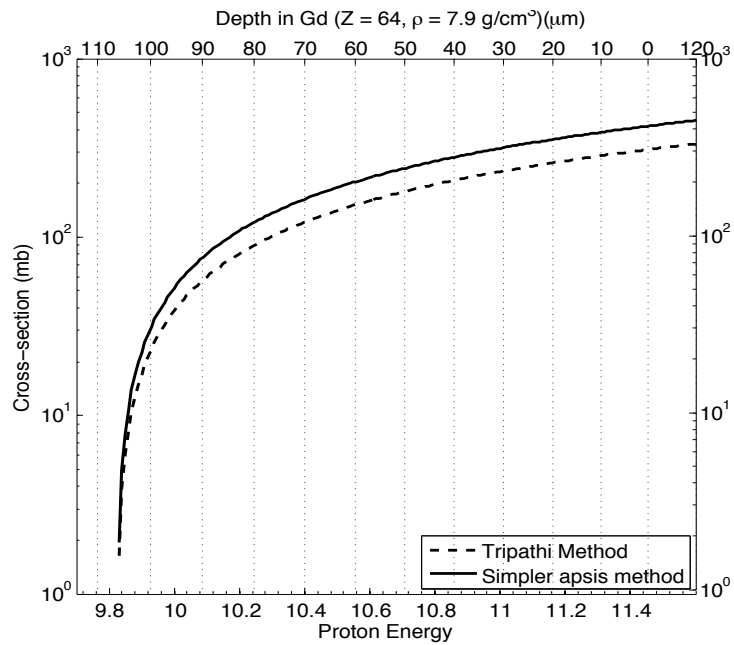
Figure 2.4: Energy Dependence of Production Cross Section. Top axis models the depth at which the beam will have the corresponding energy (bottom axis).

Coulomb barrier. We corrected the cross section to vanish at their value of the Coulomb

barrier, and plotted Equation 2.5 as a function of proton energy in Figure 2.4, along side

the Tripathi formula. The top axis models the depth at which the beam, initially at 11.6

MeV, will have the corresponding energy labeled on the bottom axis. These values were

calculated by integrating the stopping power for protons in gadolinium (7.9 g/cm^3, the

closest analog to dysprosium on the PSTAR database) in $10\,\mu$m intervals(Berger et al.,

2008). Here we can see that after a depth of about $95\,\mu$m, the cross section drops by an

order of magnitude and vanishes completely before $110\,\mu$m.

To test this idea, we attempted to perform a short, low-current bombardment with two,

100 micron foils sandwiched together and measure their activity. The experiment failed

because the heat transport was so bad that the two foils nearly melted; they fused to each

other and to the target holder rendering the result useless. Instead, we repeated the same

experiment with a single 250 micron foil followed by a single 100 micron foil. After

bombardment, each foil was placed at a fixed distance from an ion chamber and their exposure rates were recorded; the graphite caps used in each bombardment were treated similarly since, especially for shorter bombardments, the charge of protons incident on the target is not well reproducible. The ratio of each's exposure rate to its corresponding cap was compared. The results were as expected: the two foils had virtually identical production. Using the thinner of the foils would therefore decrease the amount of heat deposited in the foil, facilitating the cooling process. With this combination of water- and helium-cooling of a thinner foil, we were able to run the cyclotron at 30 μA for 3 hours without compromising the structural integrity of the foil.

The VUMC cyclotron operates at a maximum of 50 μA and delivers protons with nominal energy of 11.6 MeV. By the industry standard, this machine is obsolete; nonetheless, we are able to produce sufficient activity to be useful therapuetically. Looking forward, though, the radiopharmacy is in the process of upgrading to a PETtrace 100 (General Electric); an unshielded, 100 μA machine that will deliver protons up to 16.5 MeV (and deuterons up to 8.5 MeV). By the same approximation as above we find that the cross section will increase by a factor of three at this energy, and so this increase in proton energy alone will boost the yields. The increase in beam current, after some clever engineering in target-cooling design, will also inflate the yields. The results will both decrease the beam time (and therefore cost) to produce sufficient activation as well as relax the rush in transport currently necessary to provide sufficient activity to the patient.

A new, low-energy, narrow-band x-ray source would be uninteresting without its application in mind. We will show, however, that [161]Ho, having an energy spectrum centralized at the peak of iodine absorption, succeeds in exploiting the synergistic potential of photon

37

| First | Second | Third generation |
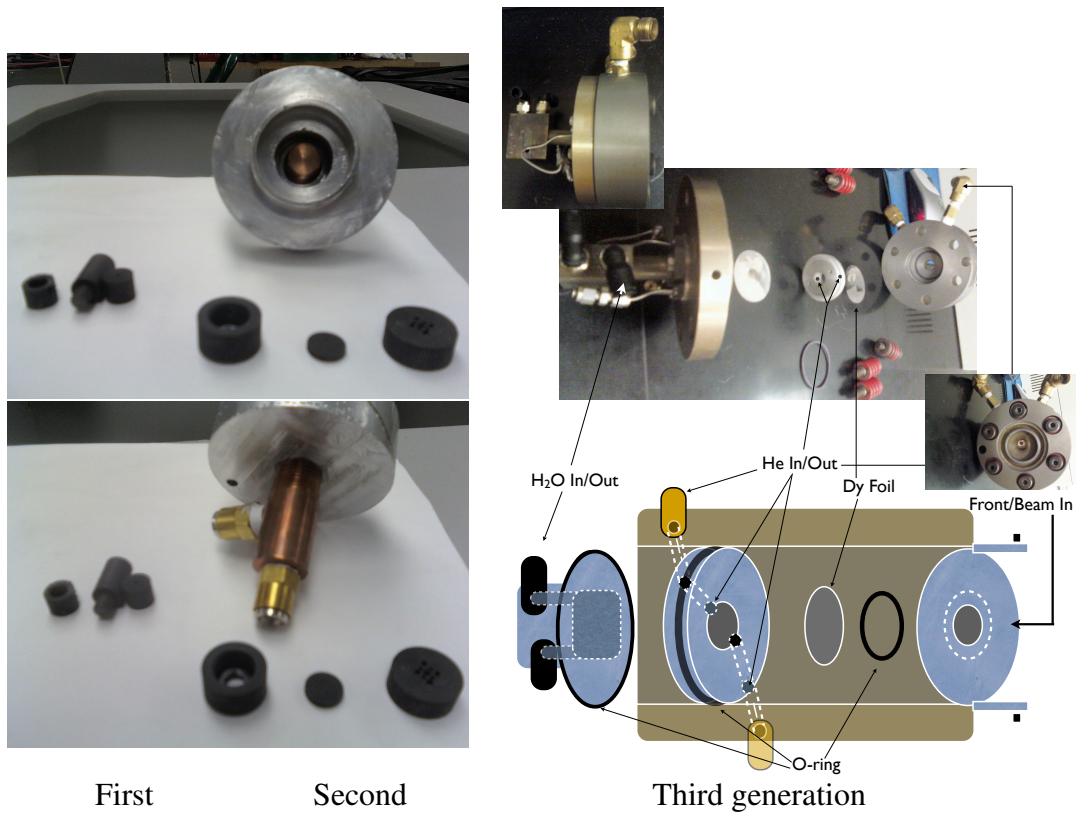
Figure 2.5: Evolution of target holder design.

activation therapy and this combination will become a more efficient technique in radiation oncology.

SENSITIZATION DEFINED

There is a need to appropriately and objectively measure sensitization based on fundamental physical processes. In the majority of literature, researchers define one of two forms of a sensitization enhancement ratio (SER): horizontal and vertical. For vertical ratios, given a particular dose, the SER is defined as the ratio of surviving fraction in the control curve to that of the drug curve (i.e. SER_{2Gy}). Horizontal values are given as the ratio of the dose required to kill a given surviving percentage in the control group to the dose required in the drug group (i.e. $SER_{10\%}$). Both of these quantities give an idea of sensitization but both depend strongly on the chosen value of dose or surviving fraction at which to measure. In fact, the vertical SER is exponentially dependent on the choice of dose, and it can be derived analytically:

$$SER_d = \frac{e^{-\alpha_2 d - \beta_2 d^2}}{e^{-\alpha_1 d - \beta_1 d^2}} = e^{-(\alpha_2 - \alpha_1)d - (\beta_2 - \beta_1)d^2} \tag{3.1}$$

where the surviving fraction, S, is related to dose, d, according to the linear-quadratic model $S = e^{-\alpha d - \beta d^2}$. Many researchers pick 2 Gy for its practical value (in fractionation therapy, 2 Gy is the usual prescription for a fraction), but otherwise this choice is arbitrary. Similarly, researchers often pick 10% survival, but different shaped curves yield wildly different ratios at different surviving levels. In Section 3.1, we construct a unified, objective way to quantify total sensitization and understand its implications in the radiobiology.

3.1 Mechanisms of Sensitization

Dose Enhancement Ratio (DER)

We need to develop the machinery to translate the radiation survival effects into physical mechanisms of sensitization. One major reason for effectiveness of IUdR is the fact that iodine, being much higher-Z material than water, absorbs radiation more effectively than water. The ratio of absorption coefficients peaks just above the K-edge of iodine, but is apparent throughout the x-ray energy spectrum. In any case, given the radiation spectrum, we can calculate how much more dose is absorbed in an iodinated medium than in water. To do so we started with the total number of photons at each energy in the radiation source. From NIST's XCOM database we collected the full mass-energy absorption coefficients $(\frac{\mu_{en}}{\rho})_E$ of air, water, and iodine, and interpolated these values at the energies of our radiation spectrum. The DER is then simply calculated as

$$DER = \sum \frac{w(\frac{\mu_{en}}{\rho})_E^{iodine} + (1-w)(\frac{\mu_{en}}{\rho})_E^{water}}{(\frac{\mu_{en}}{\rho})_E^{water}} \quad (3.2)$$

summed over all energies in the radiation spectrum, where w is the fraction by weight of the iodine in the mixture. It is generally recognized that the primary radiosensitive sites in the cell lie within the nucleus (Hofer et al., 1993; Roa et al., 1990; Narra et al., 1994) and so even though the DER of the whole cell may be greater, only the enhanced absorption in the nucleus will manifest itself in radiosensitivity. We calculated the total number of iodine atoms per nucleus from the observed moles of thymidine, moles of iodine, grams of DNA, and number of cells for each measurement in the incorporation experiments mentioned earlier in Section 4.3. Using confocal microscopy (LSM710, Zeiss) combined

40

with a Hoechst staining of the nuclei (Hoechst 33342, Invitrogen #H1339), we measured

the size of the nucleus; assuming the nucleus is a sphere of water, we calculated the volume

and therefore the mass of water in the nucleus. From this we determined w and calculated

the nuclear DER for each of our radiation sources.

Now we need to understand how this dose enhancement will manifest itself in the sur-

vival effects. Thus far we have ignored any radiobiological or chemical effects IUdR might

have on the nuclear DNA. The benefit of isolating the mechanisms of sensitization will

become more apparent later. The only thing we have included in the calculation of DER

is the fact that there is different absorption in iodine relative to water. Figure 3.1 is a con-

ceptual figure of merit that should help to visualize the effect of a DER on the survival

curve. The DER tells us that for the same air-dose (external fluence) of radiation, iodinated

nuclei will absorb an added dose. By measuring the control (no drug) response, we have

observed how an increase of dose will affect the radiation survival of the same type of cell.

So a new point (C) that is at the same surviving percentage as the dose-enhanced point B

but at an unchanged air-dose, d_1, is now on a curve for cells that have the same radiobi-

ological properties, but whose nuclei simply absorb more dose than equivalent cells with

no drug. We can see that the DER is not just a constant separation between the drug and

no-drug curves but rather an more rapid progression along the no-drug curve. This DER

is a function of the difference in absorption spectrum at all energies and as such, is dose

independent. We can calculate this new survival percentage, S_2, at every dose and generate

the new curve, both graphically and analytically. The surviving percentage at points (B)

and (C) are the same: $e^{-\alpha_1 \cdot DER \cdot d - \beta_1 \cdot (DER \cdot d)^2} = e^{-\alpha_2 d - \beta_2 d^2} = S_2$ and so solving for α and

β we are left with $\alpha_2 = DER \cdot \alpha_1$ and $\beta_2 = DER^2 \cdot \beta_1$. Again, this DER value and this new
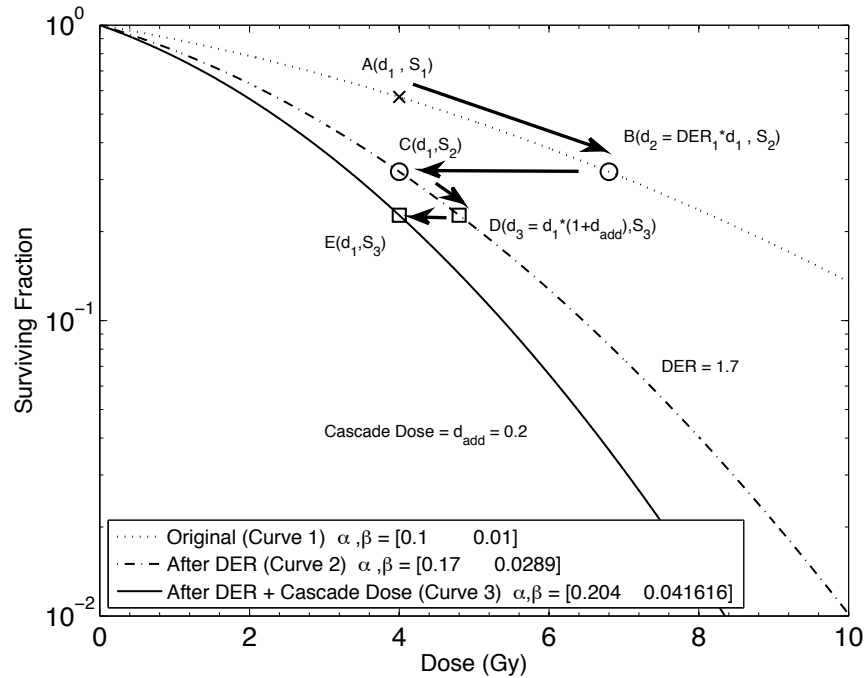
Figure 3.1: DER Visualization: A) point on control (no drug) curve at (dose, Surviving fraction) = (d_1, S_1). At same air-dose, iodinated nucleus absorbs $d_2 = d_1 \cdot DER$ whose surviving fraction is measured to be S_2 at point B. Iodination added dose without changing external fluence so drug curve goes through point C which has surviving percentage of B but air-dose of A. Similar progression from points C to E occurs from added dose due to ISI restabilization cascade.

survival curve isolates only one phenomenon: radiation is absorbed better in iodine than in water. It only takes into account the fact that there is a difference in absorbing material in the drug-containing cells relative to the control. The effect would be the same if iodine was used as a contrast agent in the nucleus and not specifically bound to anything important (i.e. DNA) in the nucleus. We must next isolate another mechanism of sensitization and understand what happens to iodine when it absorbs a photon.

Inner-Shell Ionization (ISI)

From the number of iodine atoms per nucleus and the number of cells per dish, we can use the photoelectric absorption cross-sections for iodine (Berger et al., 2005) interpolated at each energy in the radiation spectrum to calculate the total number of photoelectric events per incident photon at each energy. Using the mass-energy absorption coefficients for air we can sum over the whole spectrum and calculate the air-dose from the number of photons at each energy. This was also used later to validate the fluence and dose rate of each radiation source. Knowing the exact number of photons of each energy per dose of radiation we can calculate the total number of photoelectric events per unit dose.

The second mechanism of dose enhancement is activated after an inner-shell ionization of iodine, when the electrons reorganize themselves back to the ground state, and emit fluorescent (characteristic) x-rays and Auger electrons. Figure 3.2 shows Monte Carlo simulation results for the Auger spectrum of stable iodine after an ISI(Karnas et al., 2001). From the left plot we can see that number of electrons per ISI ranges from none (for a purely fluorescent event) to approximately 40 for an intense K-shell initiated Auger cascade, the average being nine. The variation in number and energy of the electrons among different cascades makes it difficult to calculate the dose and so we need a way to model this phenomenon and quantify the dose of radiation per ISI.

An appropriate model is ^{127}Xe which as it decays by electron capture (EC) to ^{127}I is left with an inner-shell vacancy just like stable iodine after being K-ionized. Goddu et al. (1997) have used Monte Carlo simulations to calculate the self-absorbed dose per unit cumulated activity, "S-values" for selected radionuclides including ^{127}Xe. Several source
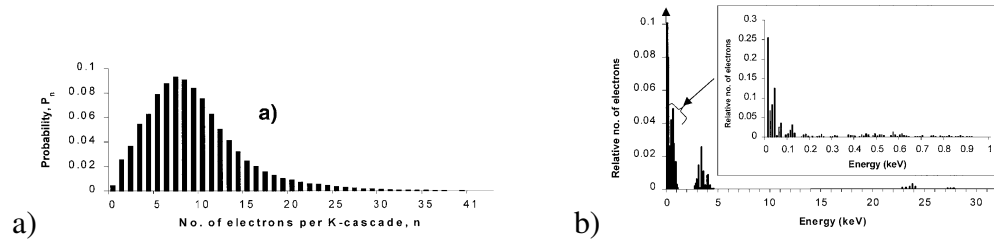
Figure 3.2: a)Histogram of the Auger distribution in terms of number of electrons ejected per initial K-shell vacancy in iodine (normalized to unity). b)Energy spectrum of emitted Auger electrons. (normalized to unity; 0.1 keV bin is truncated in main graph, but expanded in inset) Both plots from Karnas et al. (2001).

to target regions are tabulated, but for radiobiological purposes the nucleus is the most important target volume. We have measured in detail in Section 4.3 how much iodine is taken up in each compartment of the cell and so can calculate the contribution of dose from each source volume to the nucleus. Values are given as dose per disintegration of ^{127}Xe, which is equivalent to dose per ionization since during one EC decay, there is one K-shell vacancy. Thus, since we have calculated the total number of photoionizations in each target volume, we have an estimate of the added dose to the nucleus from each.

This addition of dose will this manifest itself similarly on the survival curve because the number of photoionizations increases linearly with external dose; the number of incident photons for a given radiation source is proportional to the dose. The added dose at any point will be the added dose per Gy times the dose at that point. Starting with our second curve generated after the DER calculation we have the surviving percentages, S_3, for our new curve.

$$S_3 \;=\; e^{-\alpha_2(d+d_{\mathrm{add/gy}}\cdot d)-\beta_1(d+d_{\mathrm{add/gy}}\cdot d)^2}$$

44

$$= e^{-\alpha_3 d - \beta_3 d^2} \tag{3.3}$$

where

$$\alpha_3 = (1 + d_{\text{add/gy}}) \cdot \alpha_2$$

and

$$\beta_3 = (1 + d_{\text{add/gy}})^2 \cdot \beta$$

Again, the same cells, with the same radiobiological properties, simply absorb extra dose, and we have already measured how cell survival relates to the addition of dose in the control. We have isolated and quantified two mechanisms of dose enhancement, neither of which takes into account any sensitization of the cell survival due to a foreign object attached to nuclear DNA. It is important to note that given an accurate measurement of incorporation of iodine into the different cellular compartments, this calculation will yield the *minimum* total sensitization. This concept is a useful check of the accuracy of incorporation measurement, and will be revisited later when comparing our results to those in the existing literature. Now we have to consider the effect of the higher-LET radiation that is emitted upon de-excitation (Auger and fluorescent emission) on cell survival.

Quantifying the Quality of Radiation

Notice that up to now the addition of dose to the nucleus has increased both α and β . α is a measure of intra-track, non-repairable lesions to the DNA, stemming from multiple energy depositions from the same ionizer, while β is a measure of inter-track, repairable lesions to the DNA, stemming from multiple energy depositions from different

ionizers(Fertl et al., 1984; Chapman, 1980; Malaise et al., 1987). Higher-LET radiation, by definition, is more densely ionizing and so we expect α to increase compared to low LET radiation; in general, the ratio of repairable lesions to total lesions will decrease with increasing LET. That is not to say that number of repairable lesions will decrease, because the total number of lesions will increase. The contribution of repairable lesions to total cell survival, however, should decrease with increasing LET. A measure of this effect is α/β which has units of dose; this is the dose at which both types of lesions have equal contribution to cell killing/survival. We expect this ratio to increase with increasing LET. In our case, all of the incident radiation is considered low LET, but the radiation coming from the de-excitation of the ionized iodine is much higher LET (low energy photons and electrons). The hypothesis is that an increasing number of ionized iodine atoms should result in more high-LET radiation, and that if this high-LET radiation originates in close proximity to the nuclear DNA, we should see an α-dominant survival curve. This effect should manifest itself in two ways: first, an increase of alpha $(\Delta\alpha)$ proportional to the amount of high-LET radiation that originates within an effective range of the nuclear DNA; and second, an increase of α/β from the drug- to the control-curve.

Recall that according to the mechanisms defined in Sections 3.1 and 3.1 the ratio α/β will decrease because β is increasing as the square of the dose enhancement in both cases while α increases linearly. Observation of an increase of α/β would then validate the necessity of isolating dose enhancement from radiosensitivity.

CHAPTER IV

PHARMACOLOGY AND *IN VITRO* PREPARATION

4.1   Brief History of IUdR Usage

The use of the halogenated pyrimidine, iododeoxyuridine (IUdR), as a radiosensitizers

has fallen in and out of favor since its original proposal in the 1950's for a variety of reasons

ranging from chemical and physical to practical.   Pharmacological issues have included

insufficient thymidine replacement, stand-alone cytotoxicity, and lack of specificity of drug

uptake in the tumor. Radiosensitization requires a substantial contrast of both drug uptake

and radiation absorption in the tumor relative to healthy cells.   In attempts to increase

the uptake of IUdR, increases in drug concentration had exceeded toxic levels, thereby

rendering this type of therapy futile. Tumor proliferation rates far exceed those of normal

tissues in most cases, but for some fast growing cell types (e.g. bone marrow and intenstine)

uptake has resulted in cytotoxicity, again defeating the purpose of the technique. Also, *in

vivo*, unincorporated iodine is taken up in the thyroid and accumulates in the liver. This is

the main pitfall of using radioactive ^{125}IUdR, which provides highly specific irradiation of

tumor cells with the advantage of depositing all of its dose in close proximity to the nuclear

DNA and so proving effective *in vitro*, but whose accumulation of dose in the liver proves

harmful. Fortunately, researchers have come up with clever ways to increase incorporation

while limiting cytotoxicity (e.g. thymidylate synthetase (TS) inhibitors block the pathways

of *de novo* synthesis of thymidine, thereby forcing the cell to use the IUdR pools during

replication), and so incorporation of stable IUdR has reached useful levels.

There has also been a problem efficiently activating the drug once it is incorporated. The mechanism of activation of IUdR requires an ionization of the iodine atom. This simple concept is of paramount importance when understanding what kind of radiation is necessary to provide not only sufficient activation of the drug, but significant contrast to surrounding healthy cells. Synchrotron experimentation has been performed to confirm what is already well understood physically (illustrated in Figure 4.1), that iodine is ionized most efficiently just above its K-edge (33 keV), and the peak of the absorption contrast relative to water occurs slightly higher in the spectrum at ~50 keV (Corde et al., 2004). At these energies, nearly all of the interactions are photoelectric, resulting in an inner-shell ionization (ISI). The resulting cascades of characteristic x-rays and Auger electrons are the powerful ionizers from which this type of therapy first attracted interest. These are similar to appealing effects of ^{125}IUdR therapy, but photon activation accentuates the synergy between radiation and sensitizer; unlike radionuclide therapy, there is only moderate toxicity (if any) where only the drug (or only the radiation) is present. By using low energy activation sources below the K-edge of iodine (e.g. ^{125}I, and ^{103}Pd) or high energy sources where interactions are almost exclusively Compton scattering (e.g. ^{60}Co, and MV x-rays), neither enhanced ionization nor absorption contrast is exploited. Broadband sources mask this enhancement because only a fraction of their spectrum lies in this sensitive region, while the rest deposits dose nearly equally in cells with or without the drug. In this study, we combine ^{161}Ho, a radionuclide with the appropriate energy spectrum centralized at the peak of absorption, with the iodinated drug in order to optimize the radiosensitization per unit dose of radiation.

In this study, radiation survival of HT-29 cells is measured *in vitro* after radiation with

48
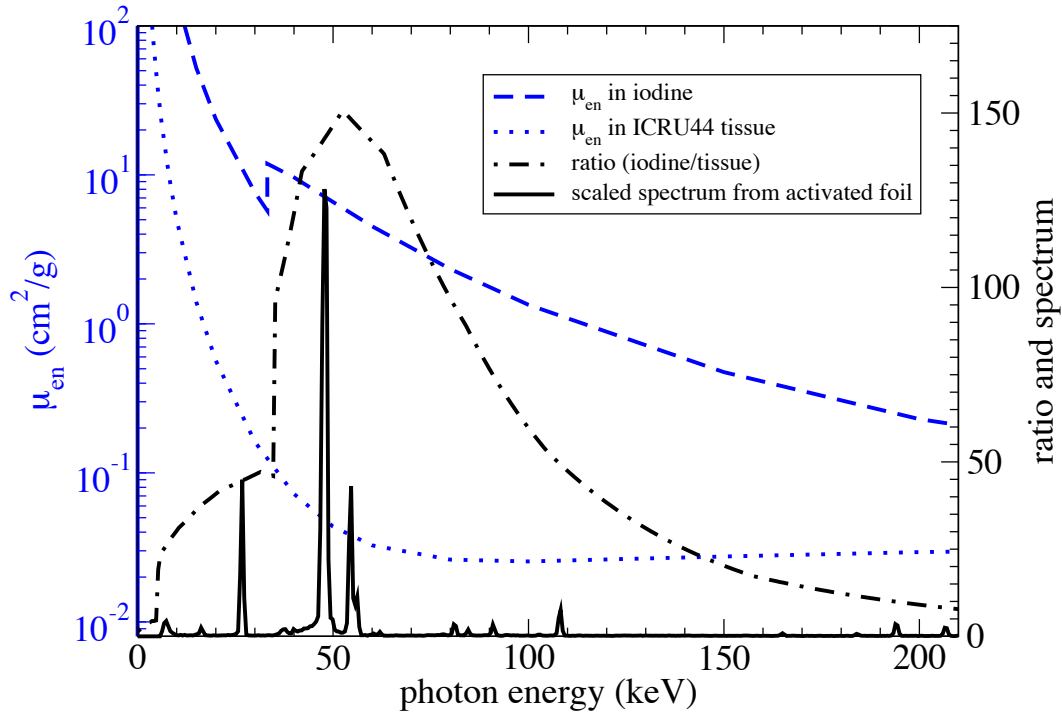
Figure 4.1: Mass absorption coefficients for water and iodine (left (log) axis) vs photon energy as well as their ratio (right (linear) axis). Also pictured is the scaled spectrum of radioactive holmium created as discussed in Section 5.2.

[125]I seeds, radioactive holmium, 300 kVp x-rays, and [137]Cs. A detailed analysis of dose deposition, in conjunction with the survival curves of each source will precede a discussion of the underlying radiobiology. Appropriate sensitization quantities will be reported for each to identify optimal photoactivation source.

4.2 Tumor Cell Line

Human colorectal adenocarcinoma (HT-29) cells (ATCC Catalog No. HTB-38) from a 44 year-old Caucasian female were maintained in McCoy's 5a Medium (ATCC Catalog No.

30-2007) supplemented with 10% v/v fetal bovine serum (ATCC Catalog No. 30-2020).

Incubation was controlled at a humidified 95% air-5% CO_2 atmosphere at 37°C. Cells were

grown in T-75 flasks, plated at a density of 2×10^4 cells/cm^2, and passaged every 4-5 days

(near 80% confluent); at this density cells would reach confluency in approximately 6 days.

For irradiation, cells were plated in a 24-well multi-well plate (CellBIND #3337, Corning

Inc., Corning, NY) in 0.75 mL of medium per well. This cell line was chosen for its noted

radioresistance (Miller et al., 1995; Kinsella et al., 1996). Progress towards radiation-

induced cell killing on this line should boost clinical interest in our method beyond merely

academic.

4.3   IUdR Incorporation Studies

Of paramount importance in quantifying sensitization enhancement is the accurate mea-

surement of the number of thymidine bases replaced by IUdR. Initially, two experiments

were done to test incorporation of IUdR into nuclear DNA. In the first, cells were plated in

T-25 flasks at various densities ranging from $1 - 4 \times 10^4$ cells/cm^2 . On the second day, each

flask was exposed to 10μM IUdR. On the third, fourth, and seventh day (i.e. 1, 2, and 5 day

exposure), one subset of two flasks was harvested, trypsinized, centrifuged, flash frozen in

liquid nitrogen, and stored at -80°C until all flasks were harvested. DNA isolation was

performed (GenElute Mammalian Genomic DNA Miniprep Kit, Sigma #G1N70(Sigma-

Aldrich, 2009a)) on the eighth day and the density of DNA in each sample was verified

by spectrophotometry. For one flask per subset, DNA was dissolved in 3% HNO_3(the pre-

ferred buffer for ICP-MS, see below). For the other flask, the sample was split into two

50

and dissolved at different densities (one twice the other) as a cross check for factors of two in the results. Also included was a baseline standard of 3% HNO_3buffer as well as a control standard of iodine containing 0.5 nM iodine. Samples were sent to the Chemical Analysis Laboratory at the University of Georgia (cal.uga) for inductively coupled plasma-mass spectrometry (ICP-MS). The second experiment was performed with each flask plated at the same density, but each exposed to a different concentration of IUdR ranging from $1 - 100\mu$M. Cells were harvested after two day exposure and handled similarly.

Another necessary detail is the knowledge of where the IUdR is incorporated in the cell. Iodine atoms in other cell compartments will affect the sensitization and therefore the survival characteristics, and so measurement of iodine in the whole cell and cell nucleus would be performed. Cells were exposed to a drug concentration of 20μM IUdR for two days. A subset of the cells was simply washed twice with PBS and vortexed in the 3% nitric acid buffer. Another subset was subject to nuclear isolation (Nuclei Isolation Kit: Nuclei EX Prep , Sigma # NUC-101 (Sigma-Aldrich, 2009b)), and complete segregation of the nuclei was verified by microscope. After centrifugation in step 4 of the protocol, the supernatant containing the cytoplasmic components including light (plasma membranes, and endoplasmic reticulum) and heavy (mitochondria, lysosomes, and rough endoplasmic reticulum) membranes was saved, dissolved in buffer, and sent along with the whole cells and isolated nuclei (also in buffer) to the chemical lab to further cross check the yields of the protocol.

Growth curves for HT-29 cells with and without exposure to IUdR are plotted in Figure 4.2. The cells conformed to exponential growth after a 1-2 day lag period, the time needed to adhere to the dish and begin signaling. Data points taken after this lag period (which can
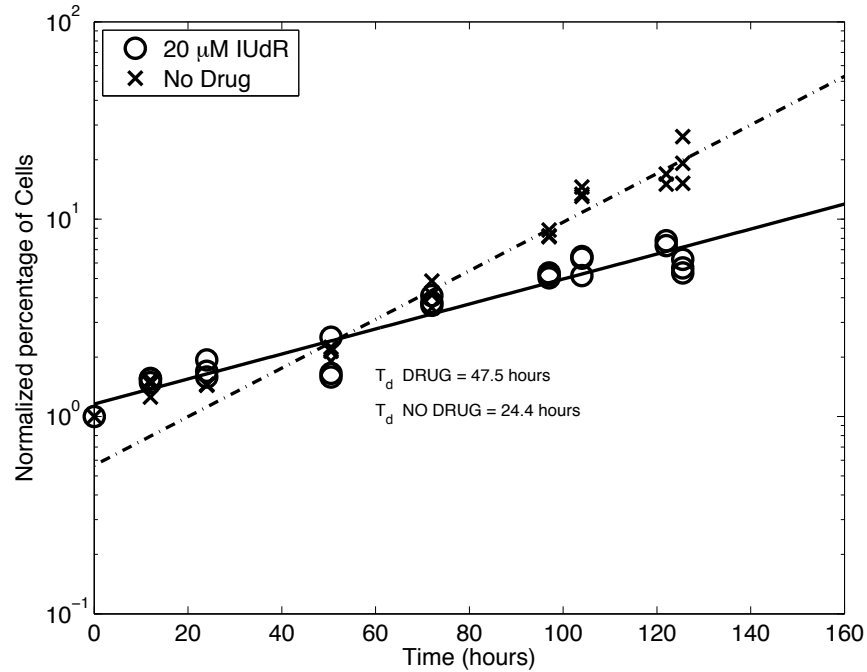
Figure 4.2: Growth Curves

be seen as the time-offset of the y-intercept) were fitted and doubling times were calculated to be 24 and 48 hours for control cells and cells exposed to 20μM IUdR, respectively.

Incorporation of IUdR into isolated, nuclear DNA is illustrated in Figure 4.3 as thymidine replacement percentage plotted against exposure time and drug concentration. Available thymidine sites were calculated from spectrophotometry of the isolated DNA, assuming 1:1 ratio AT to GC pairs and a value of 9.78×10^8 base pairs per picogram of DNA(Dolezel et al., 2003; Cavalier-Smith, 1985). Optimum incorporation was found to be 7.3% of available thymidine sites resulting from two-day exposure to $20\mu M$ IUdR. As expected, incorporation is greater after two days than after one day exposure; substitution should be largely unifilar after one DNA replication, and at least partially bifilar after the second(Fornace et al., 1990; Lawrence et al., 1990). This bifilar effect is confirmed by the factor of 1.6 increase of substitution after the first day of exposure. Exposure beyond two
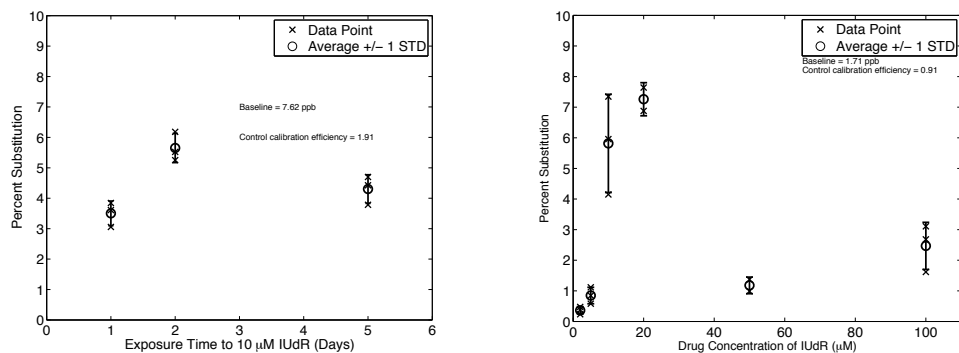
Figure 4.3: Incorporation vs time and drug concentration. Data are corrected for baseline and detector efficiency based on control samples.

doublings and to drug concentrations above $20\mu M$ introduced significant growth inhibition and cytotoxicity. Dead cells were washed away with PBS, so cells up-taking a toxic amount of drug were killed and therefore not included in the measurement. We interpret the decrease in incorporation to be a consequence of the diminished number of viable cells.

Results of the compartmental measurement of iodine are shown in Table 4.1. These results bring about two important points: first, if the DNA is not completely eluted and the concentration of DNA is not verified concurrently, calculations of incorporation percentage can vary widely; second, though not originating within the DNA double helix, Auger electrons and low energy photons coming from the ISI of iodine in the nucleus can still contribute to dose enhancement of the cells. Iodine that adheres not to the nuclear DNA, but rather to cell membranes or at other sites in the cell, acts as a contrast agent adding dose, but does not exhibit high-LET killing behavior(Corde et al., 2004). The range of these densely ionizing particles is much shorter than the dimensions of the cell, and so an Auger cascade resulting from an ISI of iodine elsewhere in the cell is unlikely to affect the DNA.

Table 4.1: Iodine measurements in various cell compartments.

per cell	Iodine Atoms ($\times 10^8$)	Percentage of Total	Dose to Nucleus per Iodine ISI (mGy)
Whole Cell	6.8	100	-
Cytoplasm†	2.0	30	0.349
Nucleus	4.8	70	3.01
Nuclear DNA	3.4	50	3.01

† Measurement includes membranes and other particulates as described in Section 4.3 and so S-value is average of cytoplasm and cell surface values.

Substitution percentages reported here are significantly lower that others have observed (Miller et al., 1995, 1992) for the same cell line and similar exposure times and concentrations. Differences reflect variability in cell culturing technique, DNA isolation, and the method of measuring iodine (e.g. NAA and HPLC). We believe our protocol to be free of major flaws and that ICP-MS is the most robust technique in iodine measurement given current technology. Also, after the first few detailed studies on incorporation , most investigators have cited the incorporation results of the original sources rather than independently measuring incorporation(Corde et al., 2004; Shinohara et al., 1996); it has been upward of 15 years since the original sources. Interpretation of cell survival will follow and should vindicate our measurements (See Chapters VII and VIII).

CHAPTER V

IRRADIATION PROCEDURES

5.1 ^{125}I Seeds

Low energy radiation below the K-edge of iodine was carried out using ^{125}I seeds (Oncoseed Model 6711, Oncura Inc., Plymouth Meeting, PA). Seed activity was verified in a calibrated, well ion chamber upon delivery and after irradiation to confirm exponential decay; dose rates between measurements were interpolated accordingly. The seed stock, which included 5 seeds of 8.49 mCi and 8 seeds of 5.64 mCi assayed upon arrival, was arranged in a 14 mm COMS eye plaque seed carrier (Trachsel Dental Studio Inc., Rochester, MN) as shown in Figure 5.1 to ensure uniform dosimetry at 0.5 cm treating distance. Dosimetry plans were carried out with Plaque Simulator 5.3.6 (BEBIG, Eckert & Zeigler, Berlin, Germany) and accounted for source decay, seed carrier attenuation, anisotropy, and irradiation geometry.

Radiation was administered by attaching the seed carrier to a plastic jig that was made to ensure 0.5 cm treating distance. Each well of the plating dish has 15.5 mm diameter and with 0.75 mL of medium the surface level is 39 mm from the cell monolayer. These dimensions are important to keep uniformity in dose as well as to ensure sterility with no contact between the seeds and the medium. Irradiation times were pre-calculated using the software, but dose was validated *in situ* by TLDs (see Section 5.5) Irradiation took place in a shielded, locked incubator to ensure proper incubation environment during longer exposures.
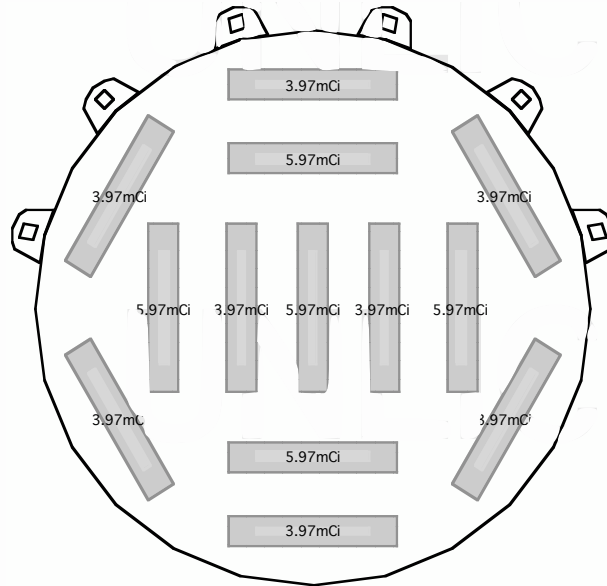
Figure 5.1: Arrangement of ^{125}I Seeds: ensures uniform dose at 0.5 cm treatment distance to within 5%.

5.2   Radioactive Holmium

Radioactive holmium was produced in the VUMC cyclotron as described in Chapter II. The helium-cooled target holder was implemented to achieve higher beam current (20 mA) and longer irradiation time (2.5 hours) without compromising the foil. Upon extraction from the cyclotron, the foil was shielded and brought to said incubator where it was attached to the same jig and fixed at 0.5 cm treating distance within one of the wells. Treatment times were estimated by ion chamber exposure rate readings upon creation, but again dose was verified by TLDs.

5.3   300 kVp X-rays

Orthovoltage x-rays were created from a PANTAK Therapax DXT 300 (Elimpex-Medizintechnik, Moedling, Austria) held at 300 kVp and 10 mA in a square, collimated 10 cm x 10 cm field

at a treatment distance of 50 cm SSD where the dose rate was calibrated to 2.2 Gy/min. The filter set consisted of 1.5 mm of aluminum and the half-value-layer was measured to be 0.75 mm of copper.

5.4 ^{137}Cs Irradiator

A 2562 Curie, ^{137}Cs source controlled pneumatically in a Mark I irradiator (JL Sheppard & Associates, Glendale, CA) with rotating turntable was used to ensure uniform dose during irradiation. The mean treatment distance was approximately 25 cm resulting in a dose rate of 1.8 Gy/min. Internal shielding limited the radiation to the 662 keV ^{137m}Ba gamma-rays.

5.5 Dosimetry

Thermoluminescent Dosimetry

Thermoluminescent dosimeters (TLDs) were used in each irradiation to verify dose. As radiation interacts with crystalline structures (LiF in our case) it causes electrons in the crystal's atoms to jump to higher energy states, where they stay trapped due to impurities (magnesium and titanium, in the case of TLD-100) in the crystal, until heated. Heating the crystal causes vibrational modes (phonons) which in turn release the trapped electrons, and they drop back to their ground state, emitting a photon of energy equal to the energy difference between the trap state and the ground state. Thermoluminescent (TL) response, measured in μC of charge, is calculated from the integral of the glow curve in the TLD-reader (Harshaw Model 3500 with WinREMS software package, Saint-Gobain Crystals &

Detectors, Solon, OH). Basically, the reader heats the TLD at a constant rate (see NOTE) and its photomultiplier tube measures the amount of light emitted at each step on the heating slope. The number of photons emitted is proportional to the number of electrons released which is ultimately proportional to the amount of dose deposited by the original radiation. Differences in LET of radiation source will lead to different patterns of dose distribution in the LiF crystals, thus necessitating an independent calibration of each radiation source (see Section 5.5).

NOTE: Recommended time-temperature profile (TTP) for 1/8"x1/8"x.035" TLD-100 chips according to user manual is as follows: preheat temperature of 50°C for 0 seconds; acquisition rate of 10°C/sec to a maximum temperature of 300°C for 33 1/3 seconds; the anneal condition is 300°C for 0 seconds, which means that the TLDs are annealed at the end of each reading automatically.

Placement

For the ^{125}I seeds and radioactive holmium, only one well of cells was irradiated at a time, and because of the proximity of the radiation source, it was important to measure the uniformity as well as the magnitude of the dose distribution to the entire well. To accomplish this, a plastic jig was made to house nine TLDs flush against the bottom of the plate. The TLDs were arranged in a 3 x 3 matrix that spanned the entire area of the irradiated well. The mean dose to the cells was calculated as the average readings of the nine TLDs. Experiments in which any individual reading was greater than 2-sigma from the mean (95% confidence interval) were discarded. For the x-ray tube and cesium irradiations, four wells
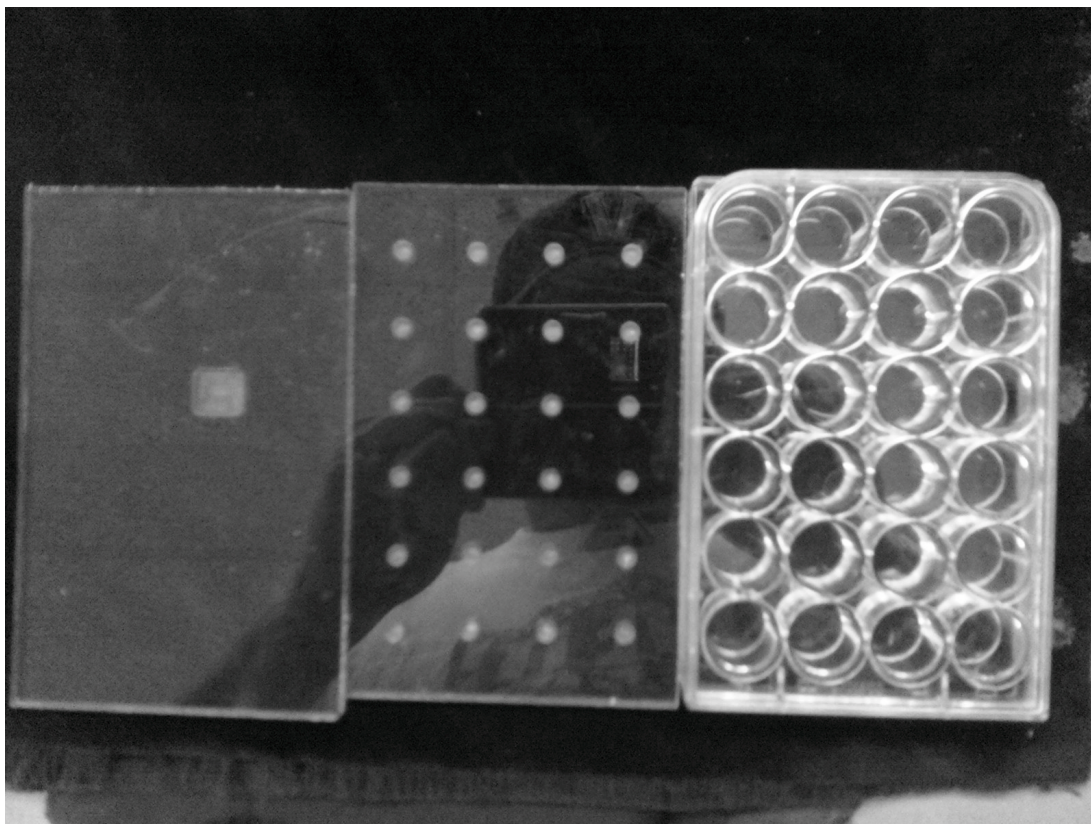
Figure 5.2: TLD housing jigs for *in vitro* irradiation. Left: jig for iodine and holmium irradiations. Cutout is just big enough to fit the 3x3 TLD configuration as well as to have full coverage of one of the wells in the culture dish. Middle: jig for cesium and x-ray tube irradiations. Cutouts are big enough to fit individual TLDs and are centered on each well in the dish. In both jigs, the cutouts are deep enough to ensure that TLDs are flush against bottom surface of dish. Right: 24-well culture dish used in all experiments.

of drug containing cells and four wells of control cells were irradiated simultaneously. To verify dose uniformity, a separate plastic jig was made to house one TLD centered on each irradiated well, flush against the bottom of the plate. Since the treatment distance for these sources is much larger, the dose uniformity within each well was not in question, especially since the dose was found to be uniform among all wells in the same plate.

Calibration

TLDs are known to have energy-dependent sensitivity(Cheunga et al., 2007; Pradhan and Quast, 2000; Meigooni et al., 1988; Jung et al., 2003). To account for this, a calibration experiment was performed for each source. Small variations exist between individual TLDs, and so each TLD was labeled and close attention was paid to ensure proper bookkeeping of each. In order to account for this variability, an element correction coefficient (ECC) was measured for each. The entire batch of TLDs (~20) were exposed to a known dose of each radiation source:

For ^{125}I and ^{137}Cs, TLDs were irradiated by point sources of each at set distances to achieve a calculable dose. (A series of experiments were done that exposed TLDs to these point sources at various distances, and therefore various dose rates, to create a sensitivity curve for the dose rate dependence, but no significant dependence was observed.) To mimic the energy and dose rate of radioactive holmium, the TLDs were irradiated by the Louisiana State University Center for Advanced Microstructures and Devices (LSU-CAMD) synchrotron at 35 keV and 0.13 Gy/min and the dose normalized to their calibration, which averaged beam-line ion chamber readings and film dosimetry values[1]. Orthovoltage x-ray tube dose was validated by ion chamber upon recent commission of the machine.

After each radiation source exposure, the entire batch was measured and their individual responses were recorded, normalized to the mean response. If an individual TLD response was more than 1-standard deviation from the group's mean response for any of the radiation sources, that TLD was discarded entirely, not to be included in any of the experiments. The ECC for each TLD was this ratio of its response to the mean. With this information, the TL

---

[1]Performed by Joseph P. Dugas. Relevant citations are (Dugas et al., 2008; Oves et al., 2008).

response can be corrected by simply multiplying the ECC by the reading (charge, q). Once each ECC has been calculated and recorded, the experiment is repeated; the symbols and error bars in Figure 5.3 illustrate the results for each radiation source. Since the TLDs were exposed to a known dose of radiation, and we know the variation in each individual TLD, we can calculate the conversion between the charge reading and the dose of radiation: the reader calibration factor (RCF) is the average slope of each source curve. Once the RCF is recorded for each radiation source we have a complete calibration, and so if TLD i is exposed to an unknown dose of radiation from radiation source j, the dose, D, can be calculated as $D = \frac{q \times ECC_i}{RCF_j}$.

The energy dependence of TL response should closely mimic the trend of absorption in the material. The inset of Figure 5.3 shows the ratio of the mass-energy attenuation coefficient of LiF to water in the relevant energy range, normalized to unity at 662 keV for the gamma ray from ^{137}Cs decay. Since LiF's absorption is higher for lower energy photons, relative to water, an over-response of TL sensitivity is expected for lower energy sources. The plotted lines on the main axes are projections of the ^{137}Cs data that have been corrected by the relative response ratio at the appropriate energy of each radiation source. Notice the data points follow the trend well and so the methodology of TL dosimetry is justified.

5.6   Radiation Survival

Cells were plated at a density of 3×10^4 cells/cm^2 in each well and incubated overnight to attach to the plate and begin in exponential growth. On the second day, half the wells
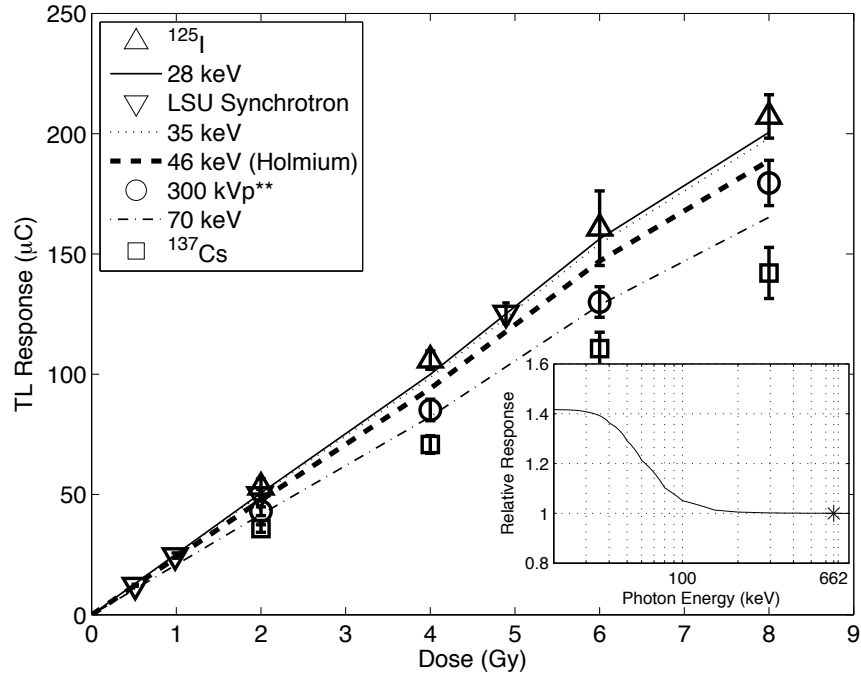
**300 kVp x-rays were filtered by 1.5 mm of aluminum and measured to have a half value layer of 0.75 mm of copper corresponding to an effective photon energy, $E_{eff} = 70$ keV ($HVL = \frac{log(2)}{\mu|_{E_{eff}}}$).

Figure 5.3: TLD energy-dependence. Symbols and error bars are the mean $\pm$ 1 standard deviation of 8 independent measurements of each radiation source at each dose. Plotted lines are theoretical projections, normalized to the ^{137}Cs response, based on the ratio of mass-energy attenuation coefficients of LiF to water taken from NIST (inset).

were aspirated of their growth medium and exposed to 20 μM IUdR (most efficient concentration for incorporation, see Section 4.3) diluted in growth medium. The other half served as the control wells, and were simply refreshed with growth medium. Cells were then left to incubate for two days (again, for highest incorporation). On the fourth day, both sets, now at 75-85% confluency, were aspirated, refreshed with growth medium, and immediately taken to be irradiated. Drug-containing medium was aspirated for two reasons: to ensure that the only IUdR available for the cells during repair was that which had bound to the DNA originally; and to limit the effects of iodine as a contrast agent, which has been

shown to cause a low-LET type background sensitization(Corde et al., 2004). For x-ray tube and cesium irradiations, one set of each (one control and one drug) was not irradiated, but still transported with the rest to exactly mimic the conditions; these were used for plating efficiency calculations. For iodine and holmium irradiations, for whichever cell set was being irradiated, a corresponding non-irradiated set was brought to the same incubator and shielded for similar plating efficiency calculations to take into account any difference in incubation environment. After irradiation, all cells were brought back to the original incubator, and left to incubate overnight to allow repair to begin. On the fifth day, each well was washed with PBS, trypsinized, centrifuged, and resuspended in 5 mL of growth medium. Cells were then plated in TC-treated, 100 mm diameter Petri dishes (Corning # 430167) at low densities (4000-10000 cells per dish) and left to incubate for 10-14 days. Three dishes were plated for each well to get sufficient statistics. Cells were then fixed with 3.7% paraformaldehyde for 5 minutes, rinsed, stained with 0.05% crystal violet, let sit for 30 minutes, then rinsed twice with tap water and drained inverted for several minutes. Colonies of 50 cells or more were counted. Colonies of less than 50 comprised of cells that have survived fewer than 5 replications and so have been sufficiently mutated to be considered non-survivors.

Statistical Analysis

Plating efficiencies were calculated for each irradiation and data were normalized to 100% survival at zero dose. Each data point consisted of the mean and variance of the three colony counts. These data were then fitted to a linear-quadratic exponential model for

surviving percentage S, $S = e^{-\alpha d - \beta d^2}$ by a weighted, non-linear least squares algorithm. The number colonies counted was, by design, high enough to keep the counting (Poisson) uncertainties on the order of a few percent. The variance was dominated by the ~10% uncertainty in hemacytometry and cell culturing, and so a constant variance of 10% was used; weights in the fit were then variance^{-1} at each point. Reduced chi-square values around unity validate this choice of weights.

CHAPTER VI

SURVIVAL COMPARISON

Radiation survival curves for irradiation of HT-29 cells by each of the radiation sources are plotted in Figure 6.1 on the same axes. Note that all of the control curves are relatively well clustered together. The LETs of our radiation sources range from $1 - 10 \frac{\text{keV}}{\mu\text{m}}$ (Makrigiorgos and Waker, 1986; Hunter and Muirhead, 2009). The relative biological effectiveness (RBE) of radiation at these values of LET are close to unity(Barendsen, 1968) and so no spread in radiation survival was expected in the controls. Data points from two other investigators (Sekhar et al. (2007) irradiated HT-29 cells with 300 kVp x-rays; Miller et al. (1987) used 250 kVp x-rays) are included to validate slope and shape of the control curves, as well as to illustrate variability between laboratories.

Sensitization, defined by any means, was smallest for ^{125}I irradiation between drug- and control-curves. This absence of an effect is dominated by the fact that almost the entire spectrum of ^{125}I falls belows the K-edge of iodine, above which the peak in absorption occurs and an inner-shell ionization is possible. Relative to water, iodine absorbs better at all x-ray energies, but above the K-edge, the ratio of absorption is greatest. Since this radiation-drug combination takes advantage of neither a difference in relative absorption, nor the added dose from an atomic re-stabilization cascade, this result comes without surprise.

Cesium irradiation brings about the second lowest sensitization among the radiation sources. Contrary to ^{125}I, radiation from ^{137}Cs decay falls entirely above the K-edge of
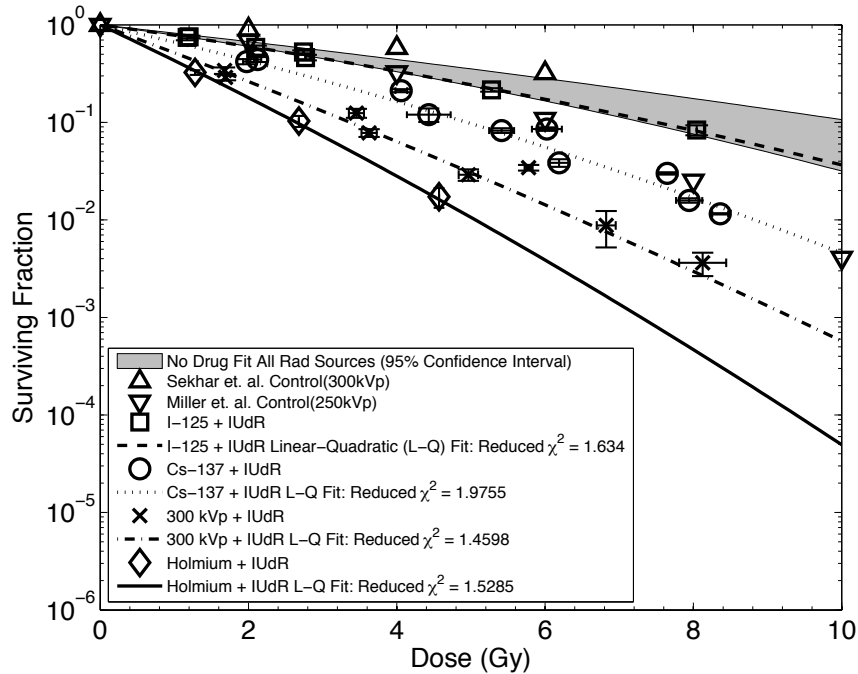
Figure 6.1: Survival curves for HT-29 cells irradiated by each radiation source, with and without 2-day exposure to $20 \, \mu$M IUdR.

iodine. The reason for a diminished sensitization is that at 662 keV, iodine's absorption is nearly identical to that of water and so the DER is near unity. Also, at this energy, almost all of the energy deposited in an iodine atom results from inelastic (Compton) scattering and so the probability of an inner-shell photoelectric ionization is minuscule. Again, given the hypothesis that IUdR is most effective just above the K-edge of iodine, this result is not unexpected.

Orthovoltage x-rays more efficiently activated IUdR because of their proximity to the K-edge of iodine. Still, because of the polychromatic nature of the x-ray tube output, the full extent of sensitization is partially masked. In fact, 9.9% of the spectrum lies below 33 keV or above 200 keV; these photons contribute 20.2% of the total dose. Below the K-edge of iodine, photons are unable to cause an ISI and therefore can not trigger the added dose

from electron re-stabilization. Above 200 keV the photoelectric cross-section for iodine falls dramatically, decreasing the probability of an ISI. This suppression of the full efficacy of photon activation therapy is the main reason for the diminished results *in vitro*, as well as in the clinic.

Radioactive holmium, whose spectrum is pictured in Figure 4.1, is our solution to this dilemma. From the survival curve in Figure 6.1, we illustrate how by selection of a photon source with the majority of the spectrum above the K-edge of iodine (but not too far as to diminish photoelectric ionization), optimal sensitization can be achieved. Using the same criteria as for the x-ray tube, 81.5% of the spectrum contributing 70.1% of the total dose fall between the 33 and 200 keV; the majority of these detrimental photons are 25.4 keV and can be filtered by design to further optimize the spectrum. Note: Copper encapsulation would be useful to conceal this low energy peak, much like titanium encapsulation of ^{125}I seeds is used to suppress beta emission.

The task remains to quantify the enhancement for each radiation source, including a thorough inspection of each dose enhancement mechanism. Table 6.1 summarizes the radiation source characteristics, dose calculations, and survival fits for each. To visualize the cumulative progression effect of each dose enhancement mechanism, we have plotted (1) the original no-drug survival curve (control), (2) the curve with only the nuclear DER added, (3) the curve with the nuclear DER plus the contribution of added dose from ISI re-stabilization, and (4) the drug curve in Figure 6.2. True sensitization beyond mere dose enhancement is isolated between curve (3) and (4). Again since SERs require arbitrary choice of the independent variable, we use the more robust measure of dose-response, $\Delta\alpha$, to understand the governing mechanism of sensitization. We note a trend in the difference

of α that is not merely dependent on mean energy of the radiation source; $\Delta\alpha$ increases as the activation energy steps past the K-edge of iodine, but then decreases beyond this energy. Recall that we hypothesized that an increasing number of ionized iodine atoms should result in more high-LET radiation, and so IUdR is most effective when activated just above the K-edge of iodine. Plotted in Figure 6.3 is the difference in α in the drug curve (4) and the theoretically dose enhanced curve (3), $\Delta\alpha$, in units of Gy^{-1} , versus the number of ionizations per Gray for each source. The trend is nearly linear with minimal offset and a slope of 0.293.

Thus far, we have not been able to quantify the decrease in β and relate it to a physical mechanism. β seems to stay nearly constant between drug and control curves, and so it could represent the inherent radioresistance of the cell line, probably owing to the efficiency of the line's DNA repair system. Also, since $\frac{\alpha}{\beta}$ is dramatically increased in the drug curve relative to the control, and the point at which dose $= \frac{\alpha}{\beta}$ is well beyond the data, this may be an artifact of the fitting procedure. In all fits except for the ^{125}I control (no-drug), however, the uncertainty in α is much less than the value of β, so the fits can be trusted, statistically. The $\alpha-$ (high-LET) dominance of the drug-containing survival curves is the central thesis of this study; it carries the most information about sensitization, leads to the most effective tumor cell killing, and in doing so, overshadows the minimal curvature effect (β-dependence).

6.1   Dose Rate Considerations

Survival effects have a known dependence on dose rate of the irradiating source. In our experiments, the initial dose rate delivered to the cell cultures ranged from 0.86 Gy/min for the ^{125}I seeds up to 1.68 Gy/min for the ^{137}Cs source. Also, with the 2.48 hour half-life of the radioactive holmium, the dose rate is exponentially decaying during irradiation. It is worth mentioning that there are established ways to account for the relative effectiveness of a given radiation prescription based on dose rate as well as the number of fractions in which the full dose is delivered. Quantities like Biologically Effective/Equivalent Dose (BED) and Relative Effectiveness (RE) have been established to, for the former, provide a way to predict the different biological effect between fractionation regimens for external beam therapy. The latter quantity provides a multiplicative correction to the dose prescription based on continuous irradiation by an exponentially decaying source. It has the form:

$$RE_\infty = 1 + \frac{R_0}{\mu + \lambda}\left(\frac{\beta}{\alpha}\right)$$

where R_0 is the initial dose rate, μ is the exponential repair constant for the relevant cell line, λ is the exponential decay constant of the radiation source, and α and β are the linear-quadratic fit parameters of the survival curve (the subscript ∞ denotes that the source is left to completely decay) (Dale, 1985). We do not speculate how this treatment would apply to our survival comparison, but rather include it for thoroughness. A diligent *in vivo* trial would certainly need to take this effect into account.
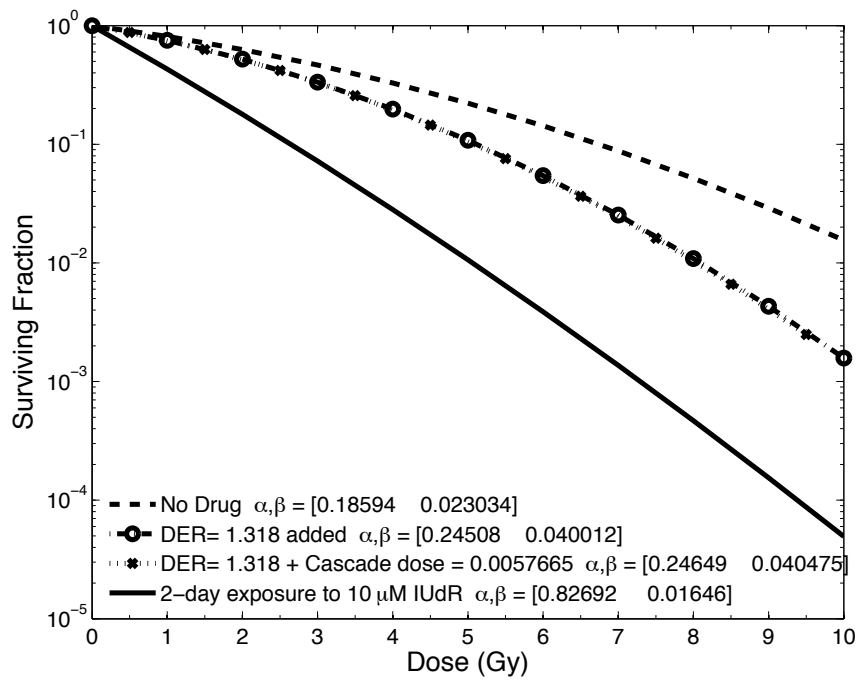
Figure 6.2: Mechanism Isolation Plot
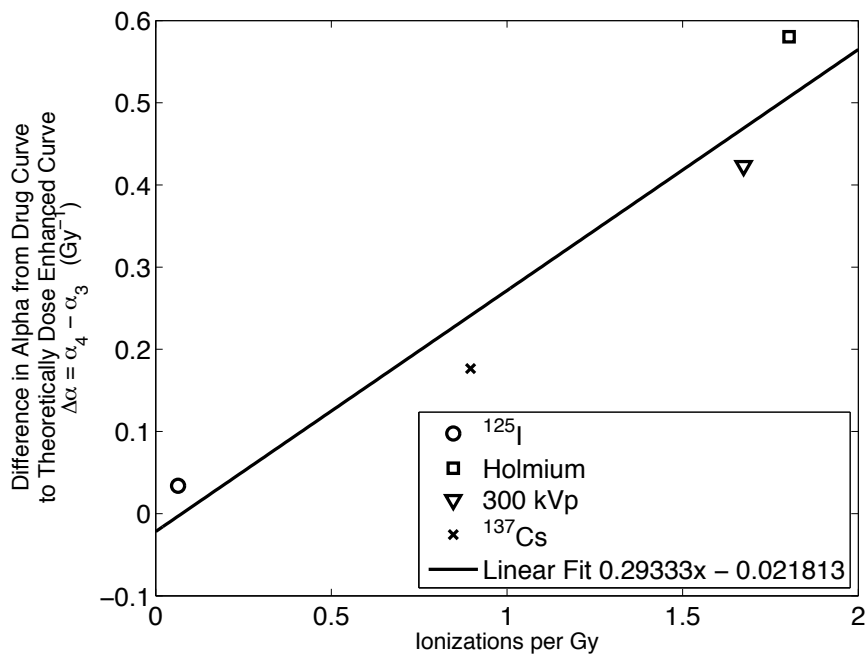
Error bars are smaller than data markers.

Figure 6.3: Determination of Ionization Contribution to α.

Table 6.1: Dose deposition and survival data.

↓ Parameter / Radiation Source →	^{125}I			^{161}Ho			300 kVp			^{137}Cs		
DER to nucleus	1.018			1.318			1.258			1.002		
$\frac{\text{K−ionizations}}{\text{nucleus·Gy}}$	0.0638			1.803			1.674			0.897		
Cascade Dose (%)	0.0415			0.577			0.535			0.287		
Fluence ($\times 10^{12}\ \frac{\gamma}{\text{Gy·cm}^2}$)	0.97			1.65			2.25			0.32		
Dose Rate ($\frac{\text{Gy}}{\text{min}}$)	.086			.121			1.64			1.68		
Mean Energy | Median Energy (keV)	28.4	27.5		72.9	46.0		83.6	62.0		661.7	661.7	
No Drug (α | β | α/β)	.198	.0144	13.7	.186	.023	8.07	.180	.0134	13.4	.216	.0105	20.7
After DER (α | β | α/β)	.201	.0149	13.5	.245	.040	6.13	.226	.0212	10.7	.217	.0105	20.6
After Cascade dose (α | β | α/β)	.201	.0149	13.5	.247	.041	6.09	.227	.0214	10.6	.218	.0106	20.6
Drug (α | β | α/β)	.235	.0095	24.7	.827	.0165	50.2	.650	.0097	67.3	.394	.0145	27.3
SER$_{2Gy}$ | SER$_{4Gy}$	1.06	1.08		3.64	13.4		2.53	6.19		1.45	2.17	
SER$_{10\%}$	1.003			2.94			2.38			1.57		
$\frac{\alpha_{\text{drug}}}{\alpha_{\text{no drug}}}$	1.19			4.41			3.62			1.82		

71

CHAPTER VII

QUANTIFYING HIGH-LET EVENTS

We need to extract some physical meaning from this trend. We have claimed that α is a measure of the number of high-LET events and that from a difference in α between the drug-curve and the dose enhanced curve ($\Delta\alpha$) we could isolate the mechanism of enhancement. But in order to support the validity of our trend, we must first identify a candidate event that leads to cell killing in such a way that mimics high-LET behavior; one such event is a double stranded break (dSB) in nuclear DNA. Studies on the cell killing mechanisms of radioactive [125]IUdR, for example, have linked the high-LET beta radiation to an increase of the number of dSBs relative to lower-LET external radiation(Kassis et al., 1987; Sundell-Bergman and Johanson, 1980; Karnas et al., 2001). The number of dSBs is not necessarily directly proportional to cell death, but it is a useful estimate of biological effectiveness (McMillan et al., 2001). But at what rate are dSBs created in cells with iodine incorporated in the nuclear DNA? Humm and Charlton (1988) calculated for iodine that 0.663 double strand DNA breaks occur per ionization cascade. Recall the interpretation of the units of our trend: we found that $\Delta\alpha$ (the most fundamental way to measure the number of high-LET events) was proportional to the number of ionizations of iodine bound to the nuclear DNA, and that the constant of proportionality was 0.293 ionizations^{-1}. This means that 29.3% of the ionizations lead to high-LET effects. Provided our calculations and those of Humm are correct, we now have an estimate of how effective dSBs are to cell killing. If 0.663 dSBs occur per ionization, and we find a contribution to $\Delta\alpha$ of 0.293 per ionization,

then on average, it takes ~2 dSB per nucleus to form enough non-repairable lesions to nuclear DNA to cause cell death (either by apoptosis or chromosomal aberrations) after two weeks of proliferation. This value fits well to the conclusions of most studies on the lethality of non-repairable dSBs. For radiosensitive cell lines, more dSBs are found per lethal death because of the inherent inability of the cell to correctly repair dSB damage (Dahm-Daphi et al., 1994; Iliakis et al., 1992). For radioresistant lines, however, the number of dSBs per lethal event approaches unity(Kysela et al., 1993; Blocher and Pohlit, 1982).

This result validates the methodology of isolating the mechanisms of cell killing enhancement: addition of dose and quality of radiation. The only thing that remains is a treatment of β. Our data show that β decreases significantly in the drug curve from the theoretically dose enhanced curves, as expected, since several repairable lesions in one cell caused by the low-LET external radiation source could be completely concealed by only one non-repairable cell-killing lesion in the same cell. In fact, this decrease in β, along with the substantial increase of α/β, is the essential validation to this theory; an increase of α alone would isolate the dose enhancement as the primary sensitization mechanism. Instead, from the dependence of $\Delta\alpha$ on the number of iodine ionizations, we see that the ionizing cascades created from these ISIs constitute the dominant mechanism.

NOTE: In our calculation of added dose to the nucleus from ISIs of iodine, we included only self absorption for a single cell and have ignored the addition of dose from adjacent cells. The data in Goddu et al. (1996) indicates a decrease of a factor of 2 in the dose absorbed in the nucleus originating in the cytoplasm relative to that which originates on the cell membrane for cells of our size. This factor of 2 gives an estimate of the distance scale of the dose distribution. We know that the range of the Auger electrons and other densely

73

ionizing particles is much less than the dimensions of the cell, and so it is reasonable to assume that ISIs of iodine atoms outside the nucleus (never mind the adjacent cells) will not contribute to dSB production. Their dose might, however, increase the total DER to the nucleus of an adjacent cell. This inclusion would slightly decrease the slope of Figure 6.3, and therefore decrease the contribution of dSBs to cell killing; the necessity of ~3-4 dSBs to cause cell death may be more plausible. Also not included in this calculation are "bystander" effects. Single particle microbeam experiments have shown that a significant number of cells that are neighbored by irradiated cells, but not themselves directly traversed by the ionizing particle, undergo chromosomal aberrations and cell death.

CHAPTER VIII

ANALYZING PAST LITERATURE

Since we have come up with a way to translate the underlying radiobiology to survival effects, we can use apply this formalism to previously reported results. Data from Miller et al. (1987) is plotted in Figure 8.1. Regrettably, the authors did not provide explicit characteristic data of the x-ray tube used other than the 250 kVp potential and 1.65 Gy/min dose rate. For consistency, we assumed similar filtering and current as our tube, and simulated the spectrum using two independent software programs: SpekCalcOSX (Poludniowski and Evans, 2007; Poludniowski, 2007) and SPEKTR (Siewerdsen et al., 2004). The simulated beam's characteristics were in good agreement using both packages and are listed in Table 8.1. Simulated dose rate was slightly lower than reported, but without knowledge of the driving current or filtration used (or the method of measurement), we could not alter this dose rate without significantly changing the shape of the output spectrum.

Since only percentage substitutions were reported, and not absolute iodine content, we also needed to simulate the iodine distribution in the cell. Again for consistency we used our measured cell size, compartmental distribution, and thymidine density and simply scaled the number of iodine atoms by the percentage replacement reported. Given the simulated x-ray spectrum and iodine distribution, we performed identical dose deposition analysis and survival curve projections; the results are tabulated in Table 8.1.

The implications of the higher substitution percentage are best illustrated in Figures 8.2 and 8.3. The main consequence of more iodine incorporation is higher absorption, which

Table 8.1: Survival data from Miller et al. (1987). Dose deposition and survival projections calculated using same analysis that produced Table 6.1

↓ Parameter / Incorporation % →	16 (0.5µM)			21 (1µM)			25 (2µM)			31 (5µM)		
DER to nucleus	1.84			2.10			2.31			2.63		
$\frac{K-\text{ionizations}}{\text{nucleus·Gy}}$	5.35			7.02			8.36			10.4		
Cascade Dose (%)	1.71			2.25			2.67			3.32		
No Drug ($\alpha\,|\,\beta\,|\,\alpha/\beta$)	0.1	.045	2.22	0.1	.045	2.22	0.1	.045	2.22	0.1	.045	2.22
After DER ($\alpha\,|\,\beta\,|\,\alpha/\beta$)	.184	.152	1.21	.210	.199	1.06	.231	.240	.962	.263	.310	.846
After Cascade dose ($\alpha\,|\,\beta\,|\,\alpha/\beta$)	.187	.158	1.19	.215	.208	1.03	.237	.253	.937	.271	.331	.819
Drug ($\alpha\,|\,\beta\,|\,\alpha/\beta$)	0.5	.035	14.3	.6	.025	15.0	.750	.025	30.0	.95	.025	17.5

Beam characteristics: Fluence: $2.16 \times 10^{12}\,\frac{\gamma}{Gy \cdot cm^2}$; Dose Rate: $1.34\,\frac{Gy}{min}$; Tube Potential: 250 kVp; Mean Photon Energy: 74.6 keV; Median Photon Energy: 59 keV; HVL: 7.59 mm Al, 0.452 mm Cu.
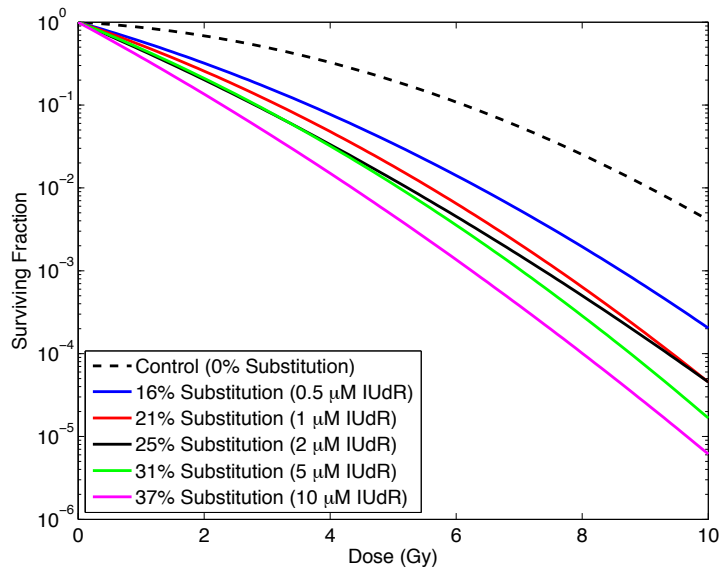
Figure 8.1: Survival Curves with several % IUdR-thymidine substitutions from Miller et al. (1987).

is quantified as the DER. Although a 250 kVp x-ray spectrum is not ideal, we see that these factors of 2-4 increase in the number of iodine atoms leads to huge DERs, which would then lead to increasingly steeper survival curve; one such projection is pictured in Figure 8.2. The dotted line is the measured control for irradiations of HT-29 cells in the absence of any drug, to various doses of the 250 kVp x-ray tube. The dot-dashed and dashed lines are the projections of the survival curve given the addition of dose stemming from the DER, and the DER plus cascade dose, respectively. Recall that these projections represent simple calculations of the fundamental physical process of absorption and as such, dictate the *minimum* sensitization effect on cell survival; they do not account for an increase of ionizing density of the Auger cascade or the introduction of a foreign object into the DNA macromolecule. The actual measurement of the drug curve, however, tells the true story. The solid line plots the survival curve of cells exposed for 2 days to 5μM IUdR leading to a measurement of 31% thymidine replacement. Notice that the measured drug curve is not nearly as steep as the calculations project it should be.
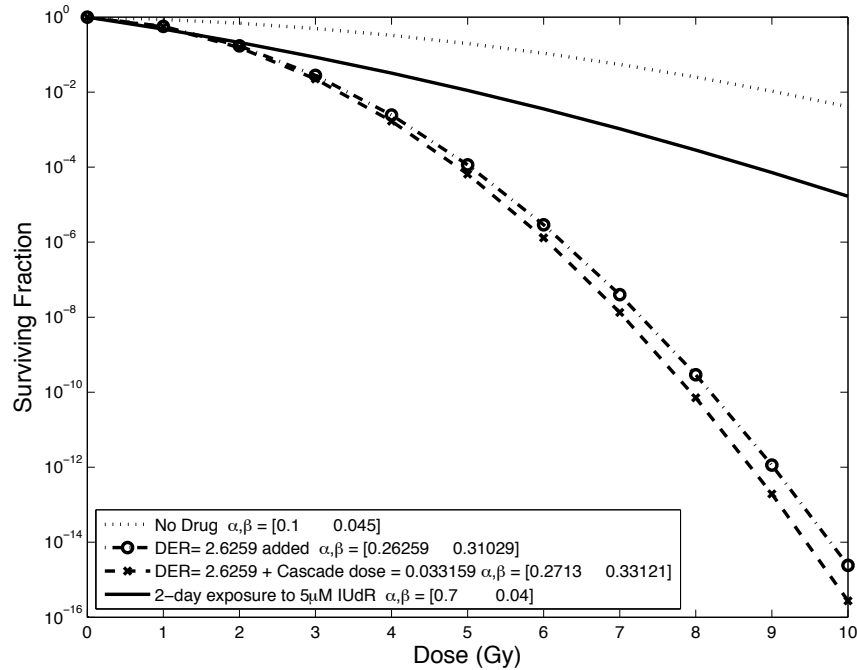
Figure 8.2: Measured vs. projected survival curve given calculated DER and Cascade Dose for 31% substitution from Miller et al. (1987).

This plot presents several interesting paradoxes. Even though the progression of α and β follow the similar pattern from control through projections to drug curves, we see for the first time that the projections are much steeper that the measured drug curves. We also see for the first time that β dominates both projections; this on its own is not contradictory since such an increase in absorption due to this high of an iodine incorporation would lead to much more low-LET radiation being absorbed in drug containing cells. We saw similar (albeit much less pronounced) increases in β with our projections, but this artifact was overwhelmed in the drug curve by a substantial increase in α that led to steeper survival curves and more efficient cell killing. Here though, the increase in α is not sufficient to dominate, which bring about another, perhaps more interesting observation illustrated in Figure 8.3.

78
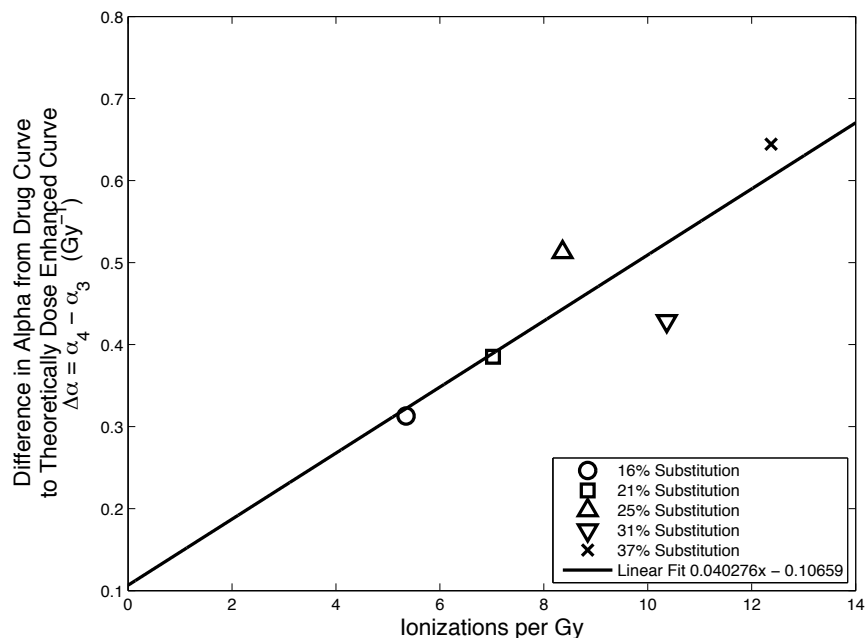
Figure 8.3: Calculated contribution of K-ionizations to α for all incorporation percentages.

When comparing the fully dose-enhanced curve to the drug curve in our analysis, we found a trend in the difference in the linear component, $\Delta\alpha$, that was proportional to the number of ISIs. This trend was logical since we hypothesized that the Auger cascade stemming from an ISI was a main source of the potency of ionization and subsequent cell killing. Also in support of this hypothesis was the proportionality constant whose unit analysis led to agreement with conclusions in relevant literature about the ballpark number of dSBs required to kill a cell. After similar analysis of the data from Miller et al. (1987), a similar trend is found. The result is a highly linear correlation, but whose proportionality constant is 0.04, more than 7 times less than the one we measured. The implications of their measurements are that it takes on average ~16 dSBs per cell to kill it, which is higher than even the strictest skeptics would estimate.

This contradiction could have one of two solutions. Our methodology could be severely

flawed, and we stumbled on the accepted value accidentally, or their incorporation measurement has overestimated the situation. Their method for measuring iodine content included elution of nucleosides by way of high pressure liquid chromatography (HPLC) and agreed well with even older studies that used neutron activation analysis (NAA: (Nath et al., 1987; Laster et al., 1993)). Given the near extinction of NAA facilities and the ubiquity of mass-spectrometry in chemical labs around the country, we stand by the claim that our measurements of absolute iodine content, and the compartmental distribution thereof, are the most accurate to date. Furthermore, our analysis of dose enhancement and sensitization is based on first-principle physics and nearly free of assumptions. We only assumed that the linear-quadratic model is the most appropriate and that each component carries physical information about the relation between the cause of cell death and the LET of the radiation that induced it. These assumptions are independently attested and have endured decades of scrutiny and remain the most popular. The only other data borrowed was from the world-renowned studies of Humm and Charlton (1988), innovators in Monte Carlo simulations of biodosimetry whose methods and conclusions remain as the basis of current models. With this in mind, we confidently claim to be fairly assessing the fundamental physical phenomena of radiation-induced cell death, and have uncovered a highly efficient method thereof to fight cancer.

CHAPTER IX

CONCLUSIONS

It should be clear that ^{161}Ho can be feasibly and inexpensively produced at sufficient activity to be useful therapeutically. Furthermore, having such a short half-life, our source would be ideal for fractionation treatment (normal prescriptions are 2 Gy per day). Commercial production of sealed seed sources (much like procedures already in place for other radioactive seeds) would lead to versatile clinical applications including matrix arrangement of seeds to cover larger treatment areas and complex, pre-planned dose distributions. We have shown that the x-rays emitted from radioactive holmium are highly appropriate for the activation of IUdR. We have isolated mechanisms of dose enhancement from each other as well as from the mechanisms of radiosensitivity, and in doing so, have extracted information about fundamental physical processes of DNA breakage. Through this independent formalism and a phenomenological assay of cell survival, we have made conclusions about the lethality of DNA dSBs that agree with the literature. Furthermore, we have developed an objective protocol to analyze sensitization effects that obviates an arbitrary choice of measurement criteria. Sensitization values from holmium irradiation reported here are by far the greatest given the uptake of our drug, even on a notably radioresistant cell line. Most importantly, since holmium is a feasible material for brachytherapy implants, the full efficacy of this combination therapy, which has gone unexploited for 60 years, can finally be realized. Our results suggest that *in vivo* studies and clinical trials of IUdR photo-activation with holmium brachytherapy merit consideration.

APPENDIX A

DER CALCULATION CODE (HOLMIUM)

```
raw_iod_data = dlmread('iodine_cross_sections.txt');
%the value in barn/atom times 1e-24 cm^2 per barn time 6.022e23 atoms per
%mol divided by XXXX (126.9 for iodine,18.015 for water) grams per mole
%gives you the value in cm^2/g
energy_iod = raw_iod_data(:,1);
photo_cm2perg_iod = raw_iod_data(:,2);
photo_barnsperatom_iod = photo_cm2perg_iod*126.9/6.022e23/1e-24;
mu_cm2perg_iod = raw_iod_data(:,3);
mu_barnsperatom_iod = mu_cm2perg_iod*126.9/6.022e23/1e-24;


raw_water_data = dlmread('water_cross_sections.txt');
energy_water = raw_water_data(:,1);
photo_cm2perg_water = raw_water_data(:,2);
photo_barnsperatom_water = photo_cm2perg_water*18.015/6.022e23/1e-24;
mu_cm2perg_water = raw_water_data(:,3);
mu_barnsperatom_water = mu_cm2perg_water*18.015/6.022e23/1e-24;


raw_air_data = dlmread('air_mass_en_absor_cm2_g.txt');
energy_air = raw_air_data(:,1);
mu_cm2perg_air = raw_air_data(:,2);


%holmium decay fits
raddata = dlmread('holmium/spec.txt');
%energy,A1,lambda1,A2,lambda2,detector efficiency
raddata = raddata(1:12,:);
radspec = raddata(:,1);


%data interpolated at radiation spectral energies
photospec_iod = interp1(energy_iod,photo_barnsperatom_iod,radspec(:,1));
muspec_iod = interp1(energy_iod,mu_barnsperatom_iod,radspec(:,1));
photospec_water = interp1(energy_water,photo_barnsperatom_water,radspec(:,1));
muspec_water = interp1(energy_water,mu_barnsperatom_water,radspec(:,1));
muspec_air = interp1(energy_air,mu_cm2perg_air,radspec(:,1));


cell_iod_data = dlmread('cell_iod_data.txt');
%iod atoms per whole cell, nucleus, cytoplasm, DNA
Iod_per_cell = cell_iod_data(1);
Iod_per_NUC = cell_iod_data(2);
Iod_per_cyto = cell_iod_data(3);
Iod_per_NUC_DNA = cell_iod_data(4);


N_cells_perdish = 5e5;
```

```
Area = 3.382;
num_iod_perdish = N_cells_perdish*Iod_per_cell;
num_cyto_iod_perdish = N_cells_perdish*Iod_per_cyto;
num_NUC_iod_perdish = N_cells_perdish*Iod_per_NUC;
num_NUC_DNA_iod_perdish = N_cells_perdish*Iod_per_NUC_DNA;
num_water_perdish = 6.022e23/18.015;
photoperphotonE_tot = photospec_iod*1e-24*num_iod_perdish/Area;
%cm2/g*g/mole*mole/atom*barn/cm2*cm2/barn*atom/cm2-->
%#photoelectric absorptions per incident photon at each energy
photoperphotonE_cyto = photospec_iod*1e-24*num_cyto_iod_perdish/Area;
photoperphotonE_NUC = photospec_iod*1e-24*num_NUC_iod_perdish/Area;
photoperphotonE_NUC_DNA = photospec_iod*1e-24*num_NUC_DNA_iod_perdish/Area;
photoperphotonE_water = photospec_water*1e-24*num_water_perdish/Area;


current = 20e-6; %in Amps
C = current*60*180;
%divide spec by charge of proton bombardment in experiment for given
%spectrum gives photons per Coloumb...then multiply by Coloumbs of charge
%during actual creation(current(Coloumbs/sec)*time(min)*60sec/min)---->
%gives total number of photons created
C_exp = 8.4538e-06;


lambda = [raddata(:,3),raddata(:,5)];
lag = 60; %lag time between end of irradiation and treatment administration
treat_d = .5; %in cm


for j=1:10


%pre-estimate exposure time necessary to achieve doses
%include lag time and decay corrections
t(j)=fsolve(@(min)j-(sum(radspec(:,1).*60./raddata(:,6)./C_exp*C.*
(raddata(:,2)./lambda(1).*(exp(-lambda(1)*lag)-exp(-lambda(1)*min))+
raddata(:,4)./lambda(2).*(exp(-lambda(2)*lag)-exp(-lambda(2)*min))).*
muspec_air)*1/4/pi*1.6e-16/33.97*1000/2.58e-4*.876*.01/treat_d/treat_d),1);


%calculate number of photons at each energy at each dose
radspec(:,j+1) = 60./raddata(:,6)./8.4538e-06*C.*(raddata(:,2)./lambda(1).*
(exp(-lambda(1)*lag)-exp(-lambda(1)*t(j)))+raddata(:,4)./lambda(2).*
(exp(-lambda(2)*lag)-exp(-lambda(2)*t(j))));


%reverify that the dose is correct
d(j)=sum(radspec(:,1).*radspec(:,j+1).*muspec_air)*
1/4/pi*1.6e-16/33.97*1000/2.58e-4*.876*.01/treat_d/treat_d;
mean_spec_energy(j) = sum(radspec(:,1).*radspec(:,j+1))/sum(radspec(:,j+1));


end


for i=1:10


dose(i)=sum(radspec(:,1).*radspec(:,i+1).*muspec_air)/4/pi*1.6e-16/33.97*1000/
2.58e-4*.876*.01/treat_d/treat_d;
%photon energy(keV)*#photons*mass_absorption(cm2/g)*1/4pi*1.6e-16 J/keV
```

divided by 33.97 J/C *1000 g/kg divided by 2.58e-4 C/kg per R times .876 rad/R
*.01Gy/rad-->Gycm2 so divide by treating distance squared gives dose in Gy

```
%ionizations per...
ion_per_cell(i)=sum(photoperphotonE_tot.*radspec(:,i+1))./N_cells_perdish;
ion_per_cyto(i)=sum(photoperphotonE_cyto.*radspec(:,i+1))./N_cells_perdish;
ion_per_NUC(i)=sum(photoperphotonE_NUC.*radspec(:,i+1))./N_cells_perdish;
ion_per_NUC_DNA(i)=sum(photoperphotonE_NUC_DNA.*radspec(:,i+1))./N_cells_perdish;

%...same only above 33 keV only
k_only_ion_percell(i)=sum(photoperphotonE_tot(2:12).*radspec(2:12,i+1))/
N_cells_perdish;
k_only_ion_percyto(i)=sum(photoperphotonE_cyto(2:12).*radspec(2:12,i+1))/
N_cells_perdish;
k_only_ion_perNUC(i)=sum(photoperphotonE_NUC(2:12).*radspec(2:12,i+1))/
N_cells_perdish;
k_only_ion_perNUC_DNA(i)=sum(photoperphotonE_NUC_DNA(2:12).*radspec(2:12,i+1))/
N_cells_perdish;

%S-values for Xe-127 r_n=4 r_C=5 microns (Gy/Bq/s)
S_N_Cy = 3.30e-4;
S_N_N = 3.19e-3;
S_C_C = 9.15e-4;

k_only_added_dose_from_cell(i)=S_N_Cy*k_only_ion_percyto(i);
k_only_added_dose_from_NUC(i)=S_N_N*k_only_ion_perNUC(i);
k_only_added_dose_to_NUC(i)=k_only_added_dose_from_cell(i)+
k_only_added_dose_from_NUC(i);
k_only_added_dose_to_cell(i)=S_C_C*k_only_ion_percell(i);
tot_num_ioniz_water(i)=sum(photoperphotonE_water.*radspec(:,i+1));

gram_per_cell = 4*pi/3*(5e-6)^3*1e6;% volume of sphere of water with 5 um radius
gram_NUC = 4*pi/3*(4e-6)^3*1e6;
gram_tot_iod = Iod_per_cell/6.022e23*126.9;
gram_NUC_iod = Iod_per_NUC/6.022e23*126.9;

%percentage iodine content
w1=gram_tot_iod/gram_per_cell;
der_tot = (w1*muspec_iod+(1-w1)*muspec_water)./muspec_water;
w2=gram_NUC_iod/gram_NUC;
der_NUC = (w2*muspec_iod+(1-w2)*muspec_water)./muspec_water;

%DER calc
tot_der(i) = sum(der_tot.*radspec(:,i+1))/sum(radspec(:,i+1));
tot_der_NUC(i) = sum(der_NUC.*radspec(:,i+1))/sum(radspec(:,i+1));

end
```

REFERENCES

Barendsen, G., 1968. Responses of cultured cells, tumors, and normal tissues to radiation of different linear energy transfer. Curr Top Radiat Res Q 4, 293–356.

Beatty, J., Biggs, P. J., Gall, K., Okunieff, P., Pardo, F. S., Harte, K. J., Dalterio, M. J., Sliski, A. P., 1996. A new iniature x-ray device for interstitial radiosurgery: Dosimetry. Med. Phys. 23, 53–62.

Berger, M., Coursey, J., Zucker, M., Chang, J., 2008. ESTAR, PSTAR, and ASTAR: Computer programs for calculating stopping-power and range tables for electrons, protons, and helium ions (version 1.2.3). `http://physics.nist.gov/Star`.

Berger, M., Hubbell, J., Seltzer, S., Chang, J., Coursey, J., Sukumar, R., Zucker, D., 2005. XCOM: Photon Cross Section Database (version 1.3)`http://physics.nist.gov/XCOM`.

Blocher, D., Pohlit, W., 1982. DNA double strand break in Ehrlich ascites tumor cells at low doses of X-rays. II. Can cell death be attributed to double strand breaks? Int J Radiat Biol 42 (3), 329–338.

Cavalier-Smith, T., 1985. The Evolution of Genome Size. John Wiley and Sons, New York.

Chapman, J., 1980. Biophysical models of mammalian cell inactivation by radiation. In: Radiation Biology in Cancer Research. Raven Press, New York, pp. 21–32.

Cheunga, T., Butsona, M., Yua, P., 2007. X-ray energy dependence of the dose response of SIRAD radiation dosimeters. Appl Radiat Isot 65, 814–817.

Commerford, S., Bond, V. P., Cronkite, E., Reincke, U., 1980. Radiotoxicity of intranuclear 125-I atoms not bound to DNA. Int J Radiat Biol 37 (5), 547–554.

Corde, S., Joubert, A., Adam, J., Charvet, A., Le Bas, J., Estève, F., Elleaume, H., Balosso, J., 2004. Synchrotron radiation-based experimental determination of the optimal energy for cell radiotoxicity enhancement following photoelectric effect on stable iodinated compounds. Brit J Can 91, 544–551.

Dahm-Daphi, J., Dikomey, E., Pyttlik, C., 1994. Relationship between non-repairable DNA strand breaks and cell survival studied in X-irradiated CHO, CHO K1, xrs1 and xrs5 cells. Int J Radiat Biol 65 (6), 657–663.

Dale, R., 1985. The application of the linear-quadratic dose-effect equation to fractionated and protracted radiotherapy. Brit J Radiol 58, 515–528.

Dolezel, J., Bartos, J., Voglmayr, H., Greilhuber, J., 2003. Nuclear DNA content and genome size of the trout and human. Cytometry Part A 51A, 127–128.

Dugas, J., Oves, S., Sajo, E., Matthews II, K., Ham, K., Hogstrom, K., 2008. Monochromatic beam characterization for Auger electron dosimetry and radiotherapy. Eur J Radiol 68 (3), S137–S141.

Faraggi, M., Gardin, I., de Labriolle-Vaylet, C., Moretti, J., Bok, B., 1994. The influence of tracer localization on the electron dose rate delivered to the cell nucleus. J. Nucl. Med. 35, 113–119.

Fertl, B., Dertinger, H., Courdi, A., Malaise, E., 1984. In vitro radiosensitivty of six human cell lines: A comparative study with different statistical models. Radiat Res 99, 73–84.

Fornace, A., Dobson, P., Kinsella, T., 1990. Enhancement of radiation damage in cellular DNA following unifilar substitution with iododeoxyuridine. Int J Radiat Oncol Biol Phys 18, 873–878.

Goddu, S., Howell, R., Bouchet, L., Bolch, W., Rao, D., 1997. MIRD Cellular S Values: self absorbed dose per unit cumulated activity for selected radionuclides and monoenergetic electron and alpha particle emitters incorporated into different cell compartments. Society of Nuclear Medicine, Reston, VA.

Goddu, S., Narra, V., Harapanhalli, R., Howell, R., Rao, D., 1996. Radioprotection by DMSO against the biological effects of incorporated radionuclides in vivo–Comparison with other radioprotectors and evidence for indirect action of Auger electrons. Acta Oncol 35 (7), 901–7.

Gutman, G., Sozontov, E., Strumban, E., Yin, F., Lee, S., Kim, J. H., 2004. A novel needle-based miniature x-ray generating system. Phys. Med. Biol. 49, 4677–88.

Hall, E., Giaccia, A. J., 2006. Radiobiology for the Radiologist, 6th Edition. Lippincott Williams and Wilkins.

Hofer, K., vanLoon, N., Schneiderman, M., Dalrymple, G., 1993. Targets for radiation-induced cell death: target replication during the cell cycle evaluated in cells exposed to x-rays or 125-I decays. Int J Radiat Biol 64, 205–216.

Hubbell, J., Trehan, P., Singh, N., Chand, B., Mehta, D., Garg, M., Garg, R., Singh, S., Puri, S., 1994. A Review, Bbibliography, and Tablution of K, L, and Higher Atomic Shell X-Ray Fluorescence Yields. J Phys Chem Ref Data 23 (2), 339–364.

Humm, J., Charlton, D., 1988. Double strand breakage in DNA produced by the photoelectric interaction with incorporated 'cold' bromine. In: Baverstock, K., Charlton, D. (Eds.), DNA Damage by Auger Electron Emitters. Taylor and Francis, London, pp. 111–122.

Hunter, N., Muirhead, C., 2009. Review of relative biological effectiveness dependence on liner energy transfer for low-LET radiations. J Radiol Prot 29, 5–21.

Iliakis, G., Mehta, R., Jackson, M., 1992. Level of DNA double-strand break rejoining in Chinese hamster xrs5 cells is dose-dependent: implications for the mechanism of radiosensitivity. Int J Radiat Biol 61 (3), 315–321.

Johns, H. E., Cunningham, J. R., 1983. The Physics of Radiology, 4th Edition. Charles C Thomas, Springfield.

Jung, H., Lee, K., Kim, J., 2003. A personal thermoluminescence dosimeter using LiF:Mg, Cu, Na, Si detectors for photon fields. Appl Radiat Isot 59, 87–93.

Karnas, S., Moiseenko, V., Yu, E., Truong, P., Battista, J., 2001. Monte carlo simulations and measurement of DNA damage from x-ray-triggered Auger cascades in iododeoxyuridine (IUdR). Radiat Environ Biophys 40, 199–206.

Kassis, A., Sastry, K., S.J, A., 1987. Kinetics of uptake, retention, and radiotoxicity of 125-IUDR in mammalian cells: implications of localized energy deposition by Auger precesses. Radiat Res 109, 78–89.

Kinsella, T., Glennon, M., Kunugi, K., M.J., L., 1996. In Viv modulation of iodoeoxyuridine metabolism and incorporation into cellular DNA by 5'-amino-5'-deoxythymidine in normal mouse tissues and two human colon cancer xenografts. Clinical Cancer Research 2, 981–989.

Kinsella, T. J., Kunugi, K. A., Wielhuber, K. A. McCulloch, W., Lio, S., Cheng, Y., 1994. An in vivo comparison of oral 5-iodo-2'-deoxyuridine and 5-iodo-2-pyrimidinone-2'-deoxyribose toxicity, pharmacokinetics, and dna incorporation in athymic mouse tissues and the human colon cancer xenograft, hct-1161. Cancer Res. 54, 2695–2700.

Krasnov, N. N., Dmitriev, P. P., Dmitrieva, Z., Konstantinov, I. O., Molin, G. A., August 1969. 13N, 11C, and 18F yields from charged particles irradiation of carbon and oxygen. Atomic Energy (Atomnaya Energiya) 27 (2), 125–128.

Kysela, B., Michael, B., Arrand, J., 1993. Relative contributions of levels of initial DNA damage and repair of double strand breaks to the ionizing radiation-sensitive phenotype of the Chinese hamster cell mutant, XR-V15B. Part I. X-rays. Int J Radiat Biol 63 (5), 609–616.

Laster, B. H., Thomlinson, W. C., Fairchild, R. G., Feb 1993. Photon activation of iododeoxyuridine: biological efficacy of Auger electrons. Radiat Res 133 (2), 219–224.

Lawrence, T., Davis, M., Maybaum, J., Stetson, P., Ensminger, W., 1990. The effect of single versus double-strand substitution on halogenated pyrimidine-induced radiosensitization and DNA strand breakage in human tumor cells. Radiat Res 123, 192–198.

Liu, D., Poon, E., Bazalova, M., Reniers, B., Evans, M., Rusch, T., Verhaegen, F., 2008. Spectroscopic characterization of a novel electronic brachytherapy system. Phys. Med. Biol. 53, 61–75.

Makrigiorgos, G., Waker, A., 1986. Measurement of the restricted LET of photon sources (5keV-1.2MeV) by the recombination method: theory and practice. Phys Med Biol 31, 543–554.

Malaise, E., Fertil, B., Deshavanne, P., Chavaudra, N., Brock, W., 1987. Initial slope of radiation survival curves is characteristic of the origin of primary and established cultures of human tumor cells and fibroblasts. Radiat Res 111, 319–333.

Mashnik, S., Sierk, A., 2002. Recent developments of the cascade-exciton model of nuclear reactions. J Nucl Sci Tech Supp. 2, 720–725.

McMillan, T., Tobi, S., Mateos, S., Lemon, C., 2001. The use of DNA double-straded break quantification in radiotherapy. Int J Radiat Onc Biol Phys 49, 373–377.

Meesungnoen, j., Jay-Gerin, J., Filali-Mouhim, A., Mankhetkorn, S., 2002. Low-Energy Electern Penetration Range in Liquid Water. Radiat Res 158, 657–660.

Meigooni, A., Meli, J., Nath, R., 1988. Influence of the variation of energy spectra with depth in the dosimetry of Ir-192 using LiF TLD. Phys Med Biol 33 (10), 1159–1170.

Mendenhall, M., 2008. `http://pythonlabtools.sourceforge.net`.

Miller, E., Fowler, J., Kinsella, T., 1992. Linear-quadratic analysis of radiosensitization by halogenated pyrimidines. Radiat Res 131, 81–89.

Miller, E., Kunugi, K., Kinsella, T., 1995. Effects of 5'-Aminothymidine and Leucovorin on radiosensitization by iododeoxyuridine in human colon cancer cells. Clin Can Res 1, 407–416.

Miller, R., DeGraff, W., Kinsella, T., Mitchell, J., Aug 1987. Evaluation of incorporated iododeoxyuridine cellular radiosensitization by photon activation therapy. Int J Radiat Oncol Biol Phys 13 (8), 1193–7.

Narra, V., Howell, R., Sastry, K., Roa, D., 1994. Auger electron emitters as tools for elucidating the location of the primary radiosensitive targets. Radiat Prot Dosim 52, 229–232.

Nath, R., Bongiorni, P., Rockwell, S., Jul 1987. Enhancement of IUdR radiosensitization by low energy photons. Int J Radiat Oncol Biol Phys 13 (7), 1071–1079.

NNDC, 2009. National Nuclear Data Center: NuDat 2.5`http://www.nndc.bnl.gov/nudat2`.

O'Farrel, T. P., Dunuaway, P. B., 1969. Effects of acute ionizing ratdiation on incorporation of 131-IUdR by cotton rats. Radiat. Res. 38, 109–124.

Oves, S., Hogstrom, K., Ham, K., Sajo, E., Dugas, J., 2008. Dosimetry intercomparison using a 35-kev X-ray synchrotron beam. Eur J Radiol 68 (3), S121–S125.

PETNET Pharmaceuticals Inc., 2002. Product Information Sheet for Metatrace FDG (Fludeoxyglucose F 18 Injection, USP).

Poludniowski, G., 2007. Calculation of x-ray spectra emerging from an x-ray tube. Part II. X-ray production and filtration in x-ray targets. Med. Phys. 34 (6), 2175–2186.

Poludniowski, G., Evans, P., 2007. Calculation of x-ray spectra emerging from an x-ray tube. Part I. electron penetration characteristics in x-ray targets. Med. Phys. 34 (6), 2164–2174.

Pradhan, A., Quast, U., 2000. In-phantom response of LiF TLD-100 for dosimetry of 192-Ir HDR source. Med Phys 27 (5), 1025–1029.

Prusoff, W., Chen, M., Fischer, P., Lin, T., Shiau, G., Schinazi, R., Walker, J., 1979. Antiviral Iiodinated Pyrimidine Deoxyribonucleosides: 5-iodo-2'-deoxyuridine; 5-iodo-2'deoxycytidine; 5-iodo-5'amino-2',5'dideoxyuridine. Pharmac Ther 7, 1–34.

Querry, M. R., Wieliczka, D. M., Segelstein, D. J., 1991. Water (H$_2$O). In: Handbook of Optical Constants of Solids II. Academic Press, pp. 1059–1077.

Roa, D., Narra, V., Howell, R., Sastry, K., 1990. Biological consequence of nuclear versus cytoplamsic decays of I-125: Cysteamine as a radioprotector against Auger cascades in vivo. Radiat Res 124, 188–193.

Segelstein, D. J., 1981. The complex refractive index of water. Master's thesis, University of Missouri-Kansas City.

Sekhar, K., Sonar, V., Muthusamy, S., Laszlo, A., Sawani, J., Horikoshi, N., Higashikubo, R., Bristow, R., Borrelli, M., Crooks, P., Lepock, J., Roti-Roti, J., Freeman, M., 2007. Novel Chelical Enhancers of Heat Shock Increase Therbal Radiosensitization through a Mitotic Catastrophe Pathway. Caner Res 67 (2), 695–701.

Seltzer, S., 1993. Calculation of photon mass energy-transfer and mass energy-absorption coefficients. Radiat Res 136 (2), 147–170.

Semnani, E. S., Wang, K., Adelstein, S. J., Kassis, A. I., 2005. 5-[123i/125i]iodo-2'-deoxyuridine in metastatic lung cancer: Radiopharmaceutical formulation affects targeting. J. Nuc. Med. 46 (5), 800–806.

Sharkey, J., Cantor, A., Solc, Z., Huff, W., Chovnick, S. D., Behar, R. J., Perez, R., Otheguy, J., Rabinowitz, R., 2002. Brachytherapy versus radical prostatectomy in patients with clinically localized prostate cancer. Current Urology Reports 3, 250–257.

Shen, W., Feng-Jun, W., Wen-long, Z., Yong-tai, Z., En-pu, F., 1989. Total reaction cross section for heavy-ion collisions and its relation to neutron excess degree of freedom. Nuc Phys A 491 (1), 130–146.

Shinohara, K., Nakano, H., Ohara, H., 1996. Detection of Auger enhancement induced in HeLa cells labeled with iododeoxyuridine and irradiated with 150 kV x-rays–Effects of cysteamine and dimethylsulfoxide. Acta Oncol 35 (7), 869–75.

Siewerdsen, J., Waese, A., Moseley, D., Richard, S., Jaffray, D., 2004. Spektr: A computational tool for x-ray spectral analysis and imaging system optimization. Med. Phys. 31 (11), 3057–3067.

Sigma-Aldrich, 2009a. GenEluteł Mammalian Genomic DNA Miniprep Kit Technical Bulletin. St Louis, MO, `http://www.sigmaaldrich.com/life-science/molecular-biology/dna-and-rna-purification/mammalian-genomic-dna-miniprep-kit.html`.

Sigma-Aldrich, 2009b. NUCLEI EZ PREP Nuclei Isolation Kit Technical Bulletin. St Louis, MO, `http://www.sigmaaldrich.com/catalog/ProductDetail.do?lang=en&N4=NUC101|SIGMA&N5=SEARCH_CONCAT_PNO|BRAND_KEY&F=SPEC`.

Sloboda, R., 2003. Dosimetric consequences of increased seed strength for I-125 prostate implants. Radiotherapy and Oncology 68 (3), 295–297.

Sundell-Bergman, S., Johanson, K., 1980. Repairable and unrepairable DNA strand breaks induced by decay of 3-H and 125-I incorporated into DNA of mammalian cells. Radiat Environ Biophys 18, 239–248.

Tripathi, R., Cucinotta, F., Wilson, J., 1997. Universal Parameterization of Absorption Cross Sections. NASA TP-3621.

Tripathi, R., Cucinotta, F., Wilson, J., 1999. Universal Parameterization of Absorption Cross Sections: Light Sesteems. NASA TP-209726.

van Dieren, E., Plaizier, B., van Lingen, A., Roos, J., Barendsen, G., Teule, G., 1996. Absorbed dose distribution of the Auger emitters 67-Ga and 125-I and the beta-emitters 67-Cu, 90-Y, 131-I, and 186-Re as a function of tumor size, uptake, and intracellular distribution. Int J Radiat Oncol Biol Phys 36 (1), 197–204.